**NTNU – Trondheim**
Norwegian University of
Science and Technology

# Fluid Inclusions in Quartz and their potential for forming a Porphyry-Cu-Mo-Deposit in the Kleivan Granite, South Norway

Silje Hatlø Hagen

Geology
Submission date: May 2012
Supervisor: Rune Berg Larsen, IGB
Co-supervisor: Bjørn Eske Sørensen, IGB

Norwegian University of Science and Technology
Department of Geology and Mineral Resources Engineering

## Abstract

The Kleivan granite is an oval granite of about 20 $km^2$ situated near Lyngdal, south Norway. It is a part of the Rogaland Igneous Complex that was formed between 1050 and 900 Ma. Samples from the quartz veins in the top of the magma chamber have been collected to investigate whether Mo might have partitioned into these quartz veins. The means of studying the quartz veins have been by optical microscopy, SEM-CL and microthermometry.

The mineral assemblage of the quartz veins consists of quartz, altered feldspars and biotite. The thin sections showing the largest fluid inclusions have been chosen for further investigation by SEM-CL and microthermometry. The SEM-CL shows the quartz as a near-homogenous phase with only occasional zonation, which indicates that the quartz in the veins have crystallized in one period only. This also indicates that all of the fluid inclusions in the samples are contemporaneous. Four different phases of fluid inclusions were found.

Evaluating the results is not an easy process, and the conclusion of the study is that more work needs to be done to make a definite statement about whether there is Molybdenum enriched in the quartz veins. .

## Sammendrag

Kleivangranitten er en 20km$^2$ stor granittpluton som ligger ved Lyngdal i Sør-Norge. Den er en del av Rogaland anortosittprovins som ble dannet mellom 1050 og 900 Ma. Steinprøver fra kvartsårene i toppen av magmakammeret har blitt samlet for å undersøke hvorvidt det finnes Mo som har partisjonert inn i disse årene. Prøvene har blitt undersøkt ved hjelp av lysmikroskopi, SEM-CL og mikrotermometri.

Kvartsårene består av kvarts, omdannet feltspat og biotitt. Tynnslipene som inneholdt de største væskeinneslutningene ble utvalgt for videre testing med SEM-CL og mikrotermometri. SEM-CL viser at kvartsen er avsatt som en homogen fase med kun tidvis sonering i kornene, noe som indikerer at kvartsen i årene har krystallisert i løpet av en enkelt periode. Dette indikerer videre at alle væskeinneslutningene i prøvene er samtidige. Det ble funnet fire typer væskeinneslutninger i prøvene.

Resultatene fra mikrotermometrien har vært vanskelige å evaluere, til det punktet at det ennå er uklart hvorvidt det finnes molybden i kvartsårene. Det anbefales derfor å bruke mer tid på undersøkelsene.

## Acknowledgements

I would like to give great thanks to all of the people who have helped me with this thesis, especially my supervisors, Professor Rune Berg Larsen and associate Professor Bjørn Eske Sørensen, for giving me their time despite their busy schedules.

I would also like to thank Nordic Mining for helping with the funding of this thesis by the means of field work in Lyngdal.

Kristian Drivenes and Morten Raanes have also been of great help with both hardware and software, and the sample preparation lab has always been ready to help me get my thin- and thick sections on time.

For immense moral support, I thank my fellow students at study hall, especially Åsa E. E. Barstad for being a great field partner, Lars Anker-Rasch for Photoshop aid, and Helene Rønning and Marte Kristine Tøgersen for great advice and reassuring words.

Last, but not least, the best motivator of them all, Magnus A. Krokstad, for pushing me through and always being there.

Brønnøysund, 30.10.2012 Silje Hatlø Hagen

# Index

# 1 Introduction

The Kleivan granite is situated near Lyngdal in South Norway, and is a pluton connected to the Rogaland Igneous Complex. With thrusting, uplifting and eroding, the pluton has come up to the surface just outside of Lyngdal, and makes up most of the landscape called Voriheia.

The pluton is an excellent example of fractioned crystallization as the lowermost part of the pluton is lying in the north and the uppermost is lying in the south beskriv bedre, efficiently making it a rather large walkthrough of the different crystallization parameters. Work has been done in this area, most worth mentioning the petrogenetic study of textures and trace elements by Dr. Francois Jacamon for his Ph.D-thesis in 2006, and Jens Konnerup Madsen and his work with fluid inclusions in 1977. Also, in the spring of 2011, Åsa E. E. Barstad wrote a MSc.-thesis about the potential for a Molybdenum mineralization in the Kleivan granite.

Nordic Mining holds the rights to the area, as it is suggested that there might be a Molybdenum enrichment in the granite because of the similarities in age and composition to the Knaben mines in Kvinesdal, South Norway, where molybdenite was extracted from the 1880's through almost 90 years (Knaben.no).

The purpose of this thesis is to investigate the fluid inclusions in the quartz veins in the top aplitic granite, to try and figure out whether there is any significant amounts of Mo in the system, and if there are, where it might be.

# 2 Regional geology

## 2.1 Magmatic processes along subduction zones

As oceanic crust is subducted under a continent into the mantle, the oceanic crust with overlaying sediments will be subjected to metamorphosis, and the basalts of the crust will be metamorphosed to amphibolites and eclogites. This might lead to a local melting because of the sinking oceanic crust or due to hot fluids extracted from the crust coming up into the overlaying mantle. A partial melting of the mantle can be the result, as the melting temperature decreases (Ramberg, Bryhni, & Nøttvedt, 2007). Figure 1 shows the principle of subduction mechanics (University of Wisconsin, 2004).

Melted rocks will move towards the surface of the Earth to relieve pressure, and whilst moving it might lead to a warming and melting of the rocks above it (Ramberg, Bryhni, & Nøttvedt, 2007). In a subduction zone, these rocks will very often be the continental crust as the oceanic crust is denser and more likely to be subducted (University of Wisconsin, 2004). This gives melts coming from different source rocks, and with different mineral compositions. The melts might mix and undergo fractional crystallization, and will end up either as plutons in the crust, or follow cracks that lead into volcanoes and then be deposited on the surface of the Earth (Ramberg, Bryhni, & Nøttvedt, 2007).

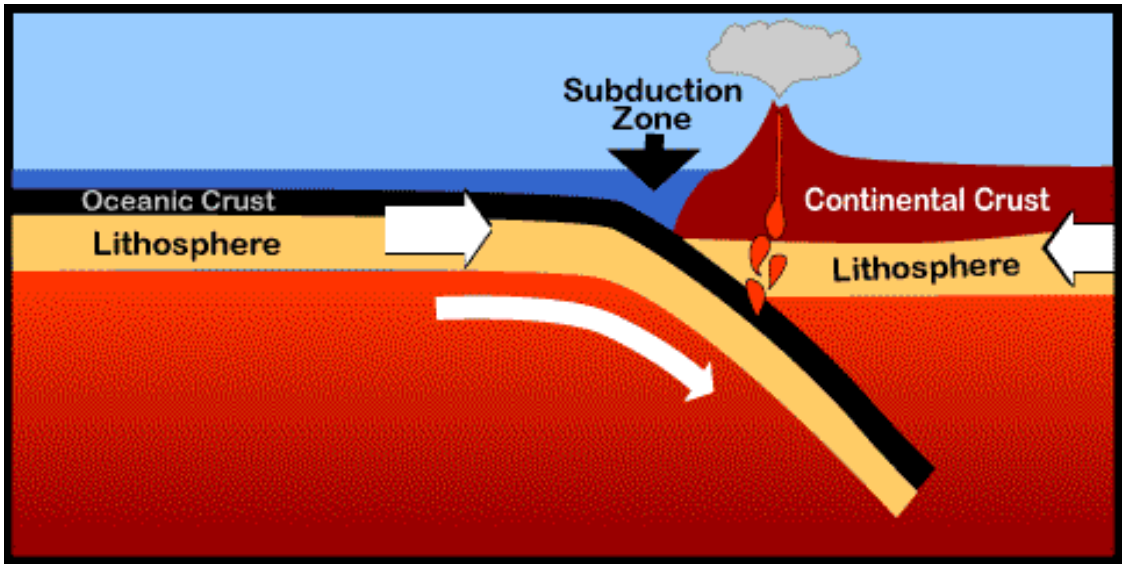


**Figure 1: Subduction principle (University of Wisconsin, 2004)**

These geological conditions were the same as in eastern Norway early in the development of the gothic mountain range, as oceanic crust was subducted under the southwestern part of the Fennoscandian shield. The gothic mountain range consists largely of granitic gneisses from

around 1660 - 1500 Ma, but metamorphosed volcanic and sedimentary rocks can also be found. The sweconorwegian orogeny led to deformation of the basal rocks, sometimes to such a degree as to form migmatites (Ramberg, Bryhni, & Nøttvedt, 2007).

## 2.2 The sweconorwegian orogeny

The better part of the basal rocks in the southern parts of Norway was formed around 1040 – 1000 Ma, after the gothic orogeny. These rocks are metamorphosed variations of originally sedimentary and volcanic deposits. The geological development ended by the formation of the sweconorwegian orogeny at 1130 – 900 Ma, when most of the rocks of South Norway were folded and subjected to rather strong deformation and metamorphosis. Some large granite bodies formed at 930 – 925 Ma, ie after the deformation and were therefore not affected (Ramberg, Bryhni, & Nøttvedt, 2007).

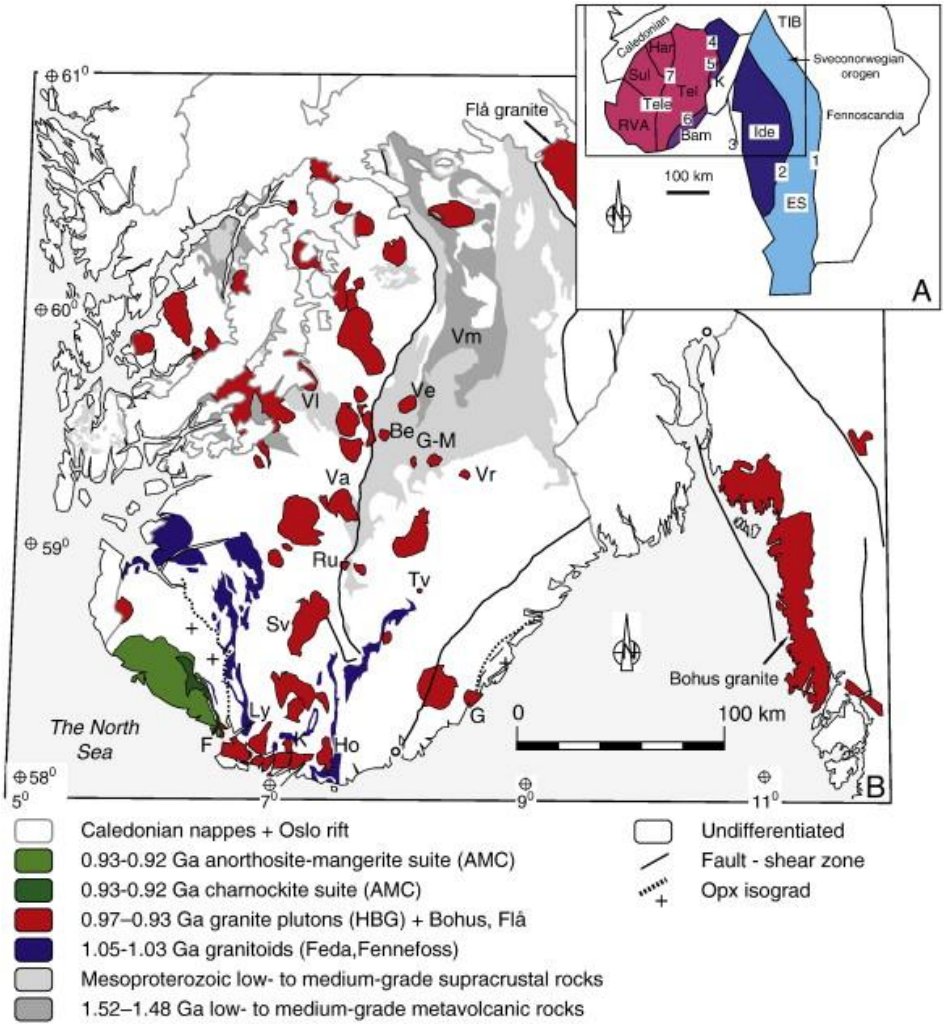


Figure 2: Overview of plutons from the sveconorwegian orogeny (Vander Auwera, et al., 2011)

Figure 2 is a cutout of a map of south Norway and southwest Sweden, and shows the different plutons that were formed during the sweconorwegian orogeny. The basal rock areas consist of several blocks of crust. These blocks are geologically distinct from each other and separated by shear zones ranging from tens of meters to some kilometers wide, oriented in a north-south or northwest-southeast direction. The deformations along the shear zones are probably caused by sideways displacement between the blocks in a late stage of the sweconorwegian orogeny. Considerable movements have occurred along some of these shear zones earlier, and some had displacement in the Permian period due to the placement of the Oslo rift (Ramberg, Bryhni, & Nøttvedt, 2007).

The sweconorwegian mountain range itself is at least 500 km wide, and developed due to plate collisions west of the Fennoscandian Shield. The south Norwegian blocks of crust displaced sideways and got attached to the gothic rocks along the western edge of the Fennoscandian Shield. The sweconorwegian mountain range is assumed to be a part of a larger, continuous mountain range system going through parts of Greenland and in to North America, where it's called the Grenville mountain range.

The first record of high P and T metamorphism was in the Bamble-Kongsberg area at 1130 – 1100 Ma, which points to an early development of a collision zone where the rocks of Bamble were pushed over the Telemark rocks along the Porsgrunn-Kristiansand shear zone. This happened roughly at the same time as the Heddal- and Bandak group was formed (Ramberg, Bryhni, & Nøttvedt, 2007).

Later in the orogenic development larger areas were the subject of deformation. The deformation appears to be strongest in the west and the south and seem to decrease towards east – northeast. The Rogaland and Vest-Agder areas were subjected to high degree metamorphosis around 1030 – 970 Ma, and in the western parts of Sweden, eclogites were formed around 970 Ma (Ramberg, Bryhni, & Nøttvedt, 2007).

Several kinds of plutons derived from the mantle or lower parts of the crusts can be found in all big mountain ranges, and these plutons are an important part of the sweconorwegian area (Ramberg, Bryhni, & Nøttvedt, 2007). The plutons are shown in Figure 2, where several groups can be distinguished based on their ages, geographical placement and composition. The two main compositions are the Anorthosite-Mangerite-Charnockite suite (AMC suite) and the hornblende- and biotite-bearing granitoids suite (HBG suite) (Vander Auwera, et al., 2011).

They are, from oldest to youngest, the Feda-Fennefoss granitoids aged 1050 to 1030 Ma, the HBG granite plutons aged 970 - 930 Ma, including the Bohus Granite now located in Sweden, and the two AMC groups of about the same age of 930 -920 Ma making up the Rogaland Igneous Province; the charnockite and the mangerite-anorthosite (Vander Auwera, et al., 2011).

The most important rocks for this study are a large number of granitic plutons aged from 990 to 925 Ma, emplaced at the end of, or right after, the orogeny. These youngest plutons are not visibly altered by the sweconorwegian metamorphosis. Some of the largest granites cover areas of several hundreds of square meters, and can be found in a belt going from south Norway up to the Hardanger plateau. These granite plutons contain a number of interesting minerals, molybdenum among others, which have been excavated from the Knaben mines in Kvinesdal. The ore consists of small specks and lumps of molybdenite, and were mined from the early 1900s until the closing of the mine in 1973 (Ramberg, Bryhni, & Nøttvedt, 2007).

## 2.3 Rogaland Igneous Complex

The RIC is a 1700 $km^2$ area consisting of several of the large plutons shown in Figure 2. The plutons are mostly comprised of anorthosite, norite and jotunite (gabbro type rocks), mangerite (a monzonite) and granite, and they are all shown in Figure 3. These plutons were formed at the end of the sweconorwegian "era" due to a melting of the mantle and the lowermost parts of the crust. The magmas cooled and solidified between 932 to 920 Ma on several kilometers' depth, at the same time as the Flå and Iddefjord granites in southeast Norway (Ramberg, Bryhni, & Nøttvedt, 2007).

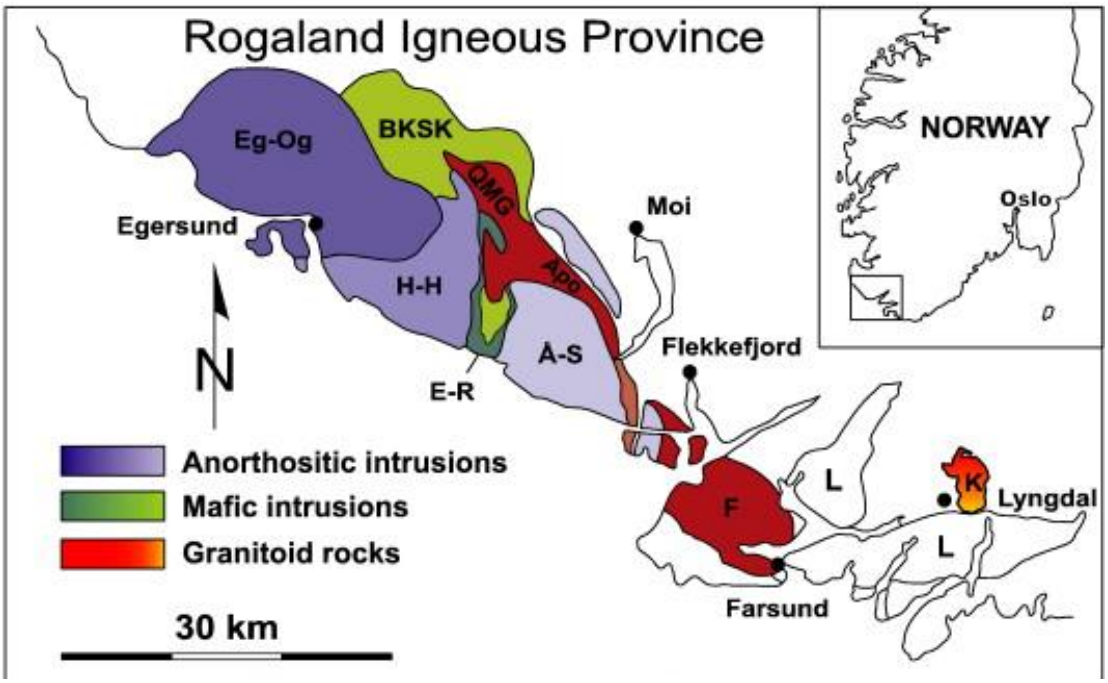


**Figure 3: Overview of the RIC. (Jacamon & Larsen, 2006)**

The RIC intrusions shown in Figure 3 are divided into three types by mineral composition and are marked with different colors. The anorthositic intrusions marked in shades of blue include the Egersund-Ogna, Helleren-Håland and Åna-Sira plutons, and are a part of the AMC suite. The mafic intrusions marked in green are the Bjerkreim-Sokndal and the Eia-Rekefjord, also from the AMC suite. The granitoid rocks are a part of the charnockite suit, meaning pyroxene bearing, and consists of the quartz mangerite (QMG). The granitoids also includes the Farsund granite (F) and the Kleivan granite (K) in the southern- and westernmost part of the RIC (Ramberg, Bryhni, & Nøttvedt, 2007).

## 2.4 The geology of the Kleivan granite

The Kleivan granite is an oval intrusion covering approximately 20 $km^2$, situated near Lyngdal, south Norway (Petersen, 1980). The Kleivan granite is a part of the RIC, separated from the Farsund Charnockite by the Lyngdal granodiorite body, and is divisible in four easily recognizable types of granite by their mineral compositions. The northernmost part of Kleivan is charnockittic, meaning pyroxene (Px) bearing, and changes southwards into a hornblende bearing granite (Hbl), then a biotite bearing granite (Bio), and finally an aplitic granite (Apl) containing some biotite and granitic pegmatites in the south. (Jacamon & Larsen, 2006b)

The Kleivan zonation is due to a slow separation of granite fractions from a convecting magma, where pyroxene, hornblende and biotite have been crystallized fractionally with the sinking temperatures of the cooling chamber. (Jacamon & Larsen, 2006a)

Figure 4 shows a map of the intrusion along with the differentiation of the chamber into the different granite types.

The Px-granite is, as mentioned, located in the northernmost part of the Kleivan intrusion and is the most primitive of the rocks found there.  Among the mafic minerals found in this granite are Fe-rich orthopyroxene, often altered and replaced by Ca-rich hornblende, as well as accessory clinopyroxene, apatite, zircon and calcite. Opaque minerals such as ilmenite can also be found. The felsic minerals found are plagioclase (andesine), perthitic alkali-feldspars and quartz. (Jacamon & Larsen, 2006b)

The Hbl-granite is found in the center of the pluton and is a transition phase between the Px-granite in the north and the more evolved Bio-granite in the south. The Px is missing here, and the mafic minerals found are mostly hornblende and accessory biotite. The felsic minerals here are more sodic plagioclases (oligoclase) and perthitic alkali-feldspars. Southwards, the hornblende is found in lesser and lesser amounts, and biotite in larger and larger amounts. In the southern part, the Bio-granite is the dominant granite type; with the biotite displaying a brown pleocroism in the northern parts, and more southwards the biotite has green pleochroism. Further south the biotite is reduced to an accessory mineral. (Jacamon & Larsen, 2006b)

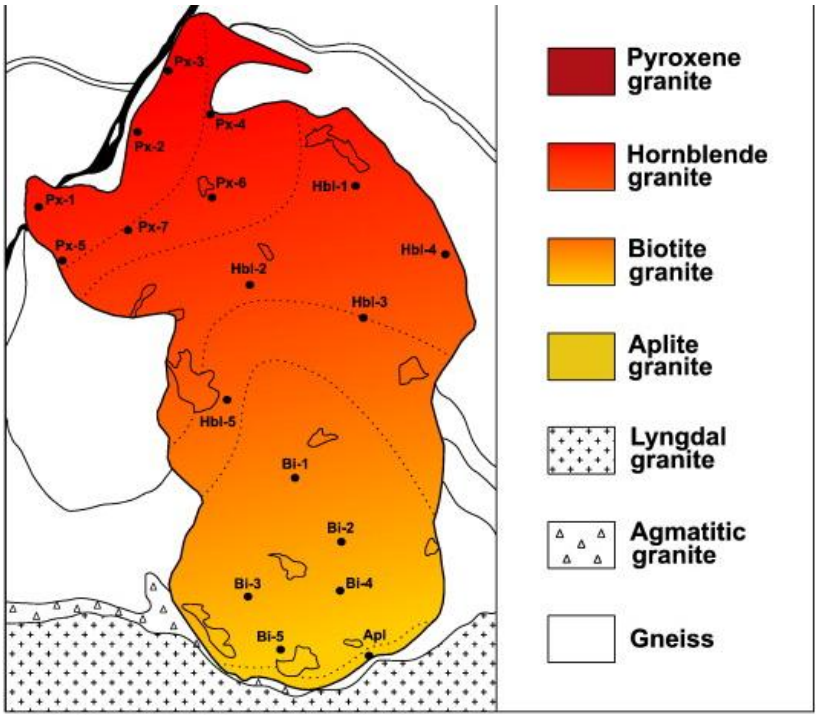


**Figure 4: Kleivan fractioned crystallization. From Jacamon & Larsen, 2006b**

The Apl-granite to the very south of the intrusion is the contact area between the pluton and the surrounding gneiss rocks, and is more of a zone of granitic, pegmatitic and aplitic rocks than a pure aplite-granite. Here, silimanite and garnets can be found as accessory minerals (Petersen, 1980)(Jacamon & Larsen, 2006a). It is also in this most evolved part of the Kleivan granite that Molybdenum (Mo) may be found, as it's an incompatible element and will be enriched in the rest melt during the crystallization of the granite. Aplite samples from a mineralization zone near the roof zone of the intrusion shows distinct manifestations of Mo. The differentiation of the granite will also favor the formation of a separate water phase enriched in incompatible elements (Barstad, 2011).

Magmatic-hydrothermal processes are the most important mechanisms for the formation of important Mo occurrences (Audétat, Dolejš, & Lowenstern, 2011), and as the roof zone of the Kleivan granite is thoroughly penetrated by quartz veins it is likely to assume that these are a result of hydrothermal activity (Barstad, 2011).

## 2.5 Previous fluid inclusion studies in the Kleivan granite

Madsen did a fluid inclusion study of 24 granite samples collected from the entire Kleivan area, and the fluid inclusions in quartz grains were analyzed. These fluid inclusions are assumed to be secondary as no distinction between primary and secondary fluid inclusions

could be found.

Three types of inclusions were found, an aqueous type, a carbon dioxide type, and a mixed type, containing visible amounts of both $CO_2$ and $H_2O$. The aqueous inclusions were two-phase liquid-gas inclusions at room temperature. Some were also observed to be one-phase liquid, especially in the southernmost, most evolved part of the granite. The inclusions varied in shape and size from irregular through to a negative crystal shape, and between 5 - 30 µm, with the irregular shapes usually belonging to the largest inclusions. In the southernmost zone, the inclusions are in general flatter, smaller and more irregular looking, and they are almost entirely confined to fractures (Madsen, 1977).

The $CO_2$ inclusions are generally smaller and more regular shaped than the aqueous ones (<10µm), and have a more well-rounded or negative crystal form. At room temperature they are found both as single phase liquid inclusions that nucleate a vapor bubble when cooled, and as two-phased liquid-gas inclusions. They are randomly distributed and also found in fractures. The mixed type are more like the aqueous inclusions in size, but are seemingly more regular in shape. They contain three phases (an example can be seen in Chapter 4 Theory, Figure 10), liquid $H_2O$, liquid $CO_2$ and gaseous $CO_2$, and are usually found in fractures throughout the granite (Madsen, 1977).

The aqueous inclusions suggests an equivalent NaCl-content between 5 and more than 23 wt%, and especially the ones in the central zone have so low final melting temperatures that it is suspected that they contain significant amounts of $Ca^{2+}$ and/or $Mg^{2+}$. A few of the inclusions found in the northern and central zones had halite crystals in them, which homogenized at around 275°C, indicating a salt content of around 36 wt% NaCl. No total homogenization was obtained, when the halite dissolved there was still 2-5 vol% gas left in the inclusion (Madsen, 1977)

# 3 Methods

## 3.1 Mapping and sampling

The samples were collected during two weeks of fieldwork in the Lyngdal municipality. The main collecting area lies in the southern, aplitic part of the granite, and samples from the network of quartz veins were prioritized.

All of the samples were registered and measured with a GPS, type Garmin GPSmap 60CSx with the local map of Lyngdal, Norway, and can be seen in Figure 5. The quartz veins were narrow, from approximately 2 to 50 cm in width, and could be followed for as short as just half a meter up to almost 15 meters towards one ravine in the north. The strategy was simply to get at least one usable sample for every quartz vein that could be found, and this is believed to have been accomplished. A list of samples can be found in Table 1.

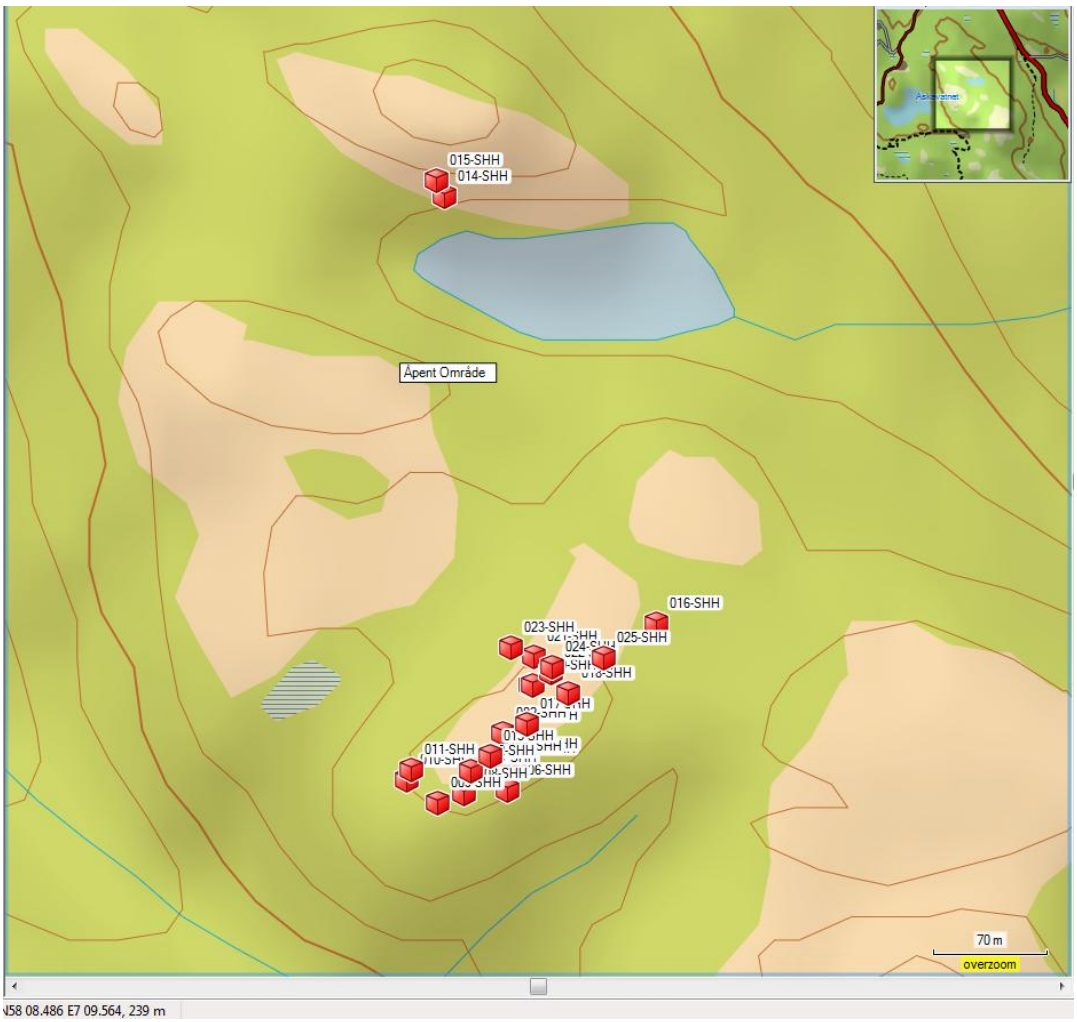


**Figure 5: GPS map of the samples taken for this study.**

The desired sample size was determined to be around the size of two fists, or the width of the quartz vein, so that it would be possible to saw it into the right shape for a thin section. It was also desirable that the samples collected were of fresh or at least just somewhat withered to avoid cracking during the sample preparation.

In the cases where tracking a vein was possible, several samples were taken throughout in case it would be interesting to note changes along the vein. Where the initial samples were small or weak, additional samples were also taken from the same vein, without discarding the first one(s), to make sure there was at least one usable sample from the vein. The total number of samples was 41, from 26 seemingly unique quartz veins. The list of samples can be found in Table 1.

It is assumed that all of the quartz veins on the surface of the aplite were sampled at least once for this study. To find the connection between the veins, strike and dip-measurements were performed where possible, and the measurements were plotted in a stereo net, see Figure 12 in Chapter 5 Results. The strike and dip measurements were done by applying the right hand rule, which means that the strike is in the direction of the index finger, and the dip in the direction of the thumb of the right hand. In addition, the direction of dip was noted.

Approximately 60 kg of quartz samples were transported by Norwegian Mail Services (Posten) from Lyngdal to Trondheim.

**Table 1: List of samples and their preparation**

| Sample | PTS | FS | Sample | PTS | FS |
|---|---|---|---|---|---|
| 001-1 | x | | 013-2 | | |
| 001-2 | | | 014-1 | | |
| 001-3 | | | 015-1 | | x |
| 001-4 | | | 016-1 | x | |
| 002-1 | x | | 017-1 | | |
| 003-1 | | | 017-2 | | |
| 003-2 | x | x | 018-1 | x | |
| 004-1 | x | | 019-1 | | |
| 005-1 | | | 020-1 | x | |
| 006-1 | x | x | 021-1 | | |
| 006-2 | | | 021-2 | | |
| 007-1 | | | 021-3 | x | |
| 008-1 | x | | 022-1 | | |
| 009-1 | x | | 022-2 | | |
| 009-2 | | | 022-3 | x | |
| 009-3 | | | 023-1 | | |
| 009-4 | x | | 023-2 | x | x |
| 010-1 | x | | 024-1 | x | |
| 011-1 | | | 025-1 | x | |
| 012-1 | x | x | 026-1 | | |
| 013-1 | | | Total | 18 | 5 |

## 3.2 Sample preparation

The first step after apprehending the samples was to start choosing which samples to process. First, all of the 41 samples were sawn in half, both as the first step of further sample preparation, and also to get a better visual impression of what each quartz vein could offer in the means of purity, cracks, accessory minerals and size.

Some of the samples were discarded due to cracking during transport or weathering, as it would be difficult to make proper polished thin sections (PTS) from them. Some were also chosen not to be processed due to the proximity to other samples or being from the same vein. Checking for consistency within veins was not prioritized at this point. Considering this, the remaining 20 best samples were chosen for PTS, and were prepared by the sample preparation lab at the Department of Geology and Mineral Resources Engineering (IGB) at NTNU. Two were discarded by the sample preparation lab due to excessive cracking. These samples were not replaced.

## 3.3 Microscopic analysis

The 18 samples were evaluated petrographically by optical microscopy, focusing on mineralogic composition, inter-and intragranular textures, and most importantly, in which PTS the largest, most primary-looking fluid inclusions could be found. The microscope used for these analyses was a Leica DM 2500 P with magnifications from 25 – 500x. Most of the photographs were taken with a ProgRess speedXT core5 with ProgRess CapturePro v.2.8.0 software.

In addition, two samples from the surrounding aplite were used for comparisons. These samples were collected by Dr. Francois Jacamon for his Ph.D-thesis (Jacamon, 2006). These samples were already prepared as PTS and FS (Fluid thick Sections). The rock itself was not available.

After the petrographic analysis, five samples were chosen for further examination due to their relatively high amount of large (5-15 µm) fluid inclusions, and the samples were prepared as FS by the sample preparation lab at IGB, NTNU. The FS were prepared as 300µm thick samples, and detached from the glass plate.

The five FS were then further examined with the same optical microscope for fluid inclusions, and the best areas with the largest and seemingly most primary fluid inclusions were marked and analyzed by SEM-CL, to check for secondary mineral growth or other indications of non-primary fluids.

## 3.4 SEM-CL

A Scanning Electron Microscope - CathodoLuminescence (SEM-CL) was utilized to discover growth zones in the quartz, to investigate whether there were any correlation between the cracks in the FS and the fluid inclusions near them, and also to compare them to fluid inclusions located inside the quartz grains.

The instrument used was the JEOL JXA-8500F Electron Probe Micro Analyzer (EPMA) at NTNU, Trondheim, Norway, and the operator was Morten Raanes. The EPMA combines high SEM resolution with high-quality X-ray analysis of sub-micron areas. This EPMA can analyse 5 elements by WDS (wavelength dispersive X-ray spectrometers) and 16 elements by EDS (energy dispersive X-ray spectrometer) simultaneously, in addition to collecting image signals from backscatter and secondary electron detectors (NTNU, 2008).

Specifications for the samples in this study were:

- Acceleration voltage: 20kV
- Beam current: 20 nA
- Probe diameter: 2 um
- Al- detection: TAPH crystal and
- Ti-detection: PETH crystal (Raanes, 2012).

Both the PTS and FS were coated with carbon, and analyses were performed on unspecified areas in the PTS, and on pre-chosen areas in the FS. The areas were, for the PTS, made 4 x 4 mms in each section, and both CL- and backscatter-images were produced under identical circumstances. For the second round, a higher resolution in the images was sought after, so the image sizes were approximately 1 x 1 mm. The images were recolored with the xCLent III Image software by CSIRO (2010).

Since the FS were detached from the glass plate by the preparation lab, they had to be attached again to go through the SEM-CL. This was done manually by applying a big drop of blank nail polish on a glass plate, and rubbing the FS carefully into it until level and attached to the glass plate. After processing, the FS was again detached by dissolving the entire glass plate and FS in acetone overnight in a small bowl with a lid, and then carefully separating them and cleaning the remaining nail polish off with more acetone and paper towels.

## 3.5 Microthermometry

The FS had already been examined by optical microscope, but after the SEM, additional pictures were taken both of the general area and of the fluid inclusions within. Most of the fluid inclusions photographed were also analyzed for the liquid/vapor ratio in Photoshop CS5, assuming that the area ratio would be a good approximation of the volume ratio.

Other methods attempted for finding the liquid/vapor-ratio in the fluid inclusions were making a "box" out of the area of the inclusion multiplied by the depth of the inclusion. The depth was measured in steps on the focus knob on the microscope and multiplying with the experimental ratio to gain the result in millimeters. The experimental ratio was obtained by drawing two dots on each side of a see-through glass plate, measuring the number of steps with the microscope, and measuring the thickness of the plate with a digital caliper. For this, the vapor bubble at room temperature was approximated as a sphere based on the measured diameter.

For the microthermometric analyses, a Linkam THMSG 600 attached to an optical microscope, type Nikon Eclipse E600 was utilized, along with Linksys 32 software for the Linkam, and Pixelink PL-A662 for the microscope. The cooling agent was liquid nitrogen with a cooling potential of down to approximately -196˚C. The slices of sample were broken into a size that would fit the circular chamber, and inserted.

Most of the fluid inclusions (FI) were cooled down to -190˚C (not all, see Chapter 3.7), and then heated by approximately 20 degrees per minute until 20 degrees before the anticipated phase transition. The heating process would slow down gradually so that the inclusion was heating at approximately one degree per minute at the time of the phase transition. This was evaluated to give a reasonable reaction time, giving an accuracy of approximately 0,1˚C (Personal message, Drivenes, 2011). All of the cooling experiments were performed first for each FS, then the heating experiments were started for that particular FS. The reason for this was to avoid accidental decrepitation.

For the heating experiments, as many as possible of the fluid inclusions were followed at the same time, but no intended decrepitations were performed before all of the inclusions had been measured. This was unlike the cooling stages, where first and final melting would have to be monitored carefully not to miss anything, so only one, or at most two, fluid inclusions could be measured at the same time. If the exact temperature was missed, the inclusion would

have to be refrozen, preferably down to -190˚C again to avoid undercooling which might produce a false reading.

For the heating stage, there is the indication of the Brownian motions of the $CO_2$, which makes it easy to monitor when one inclusion suddenly becomes "still". If the exact temperature was missed, it was a small task to cool the inclusion by approximately 30 degrees to make the $CO_2$ precipitate.

## 3.6 HMS

The mandatory safety equipment used for these experiments was safety goggles when pouring liquid nitrogen into the container for the Linkam Stage. For the sample preparations with the use of a core saw, safety goggles, thick rubber gloves, iron-tipped shoes, a dust mask, a jumpsuit and a rubber apron was worn.

Additionally, a mandatory "HMS in the lab" online course created for NTNU was attended and passed (trainor.no, 2011).

## 3.7 Sources of error

For this thesis, a lot of mistakes have already been made, which will influence the final outcome.

In the sampling, one source of error is the right hand rule. After a while of measuring, it was discovered that the left hand rule had been applied instead, simply because the right hand held the compass. For some of the results, direction of dip had also been noted, so the results could be corrected when clear-minded and back in the office, but for the ones where direction of dip were not noted, it is impossible to know whether the left- or right hand rule has been applied.

In the Table 3.1 it can also be noted that some of the strike and dip measurements lack the dip. That is simply because some of the quartz veins were entirely flat against the aplite, so there were no surfaces to measure this on. In this event, the compass was aligned along the strike direction of the vein, and the dip direction was guessed from visual clues. In retrospect, it could have been better to drop the measuring altogether, but out in the field it was helpful for distinguishing one vein from the other.

The software for the GPS did not give the actual coordinates of the sample points as a readout when connected to the computer, so there exists a map, but there are no coordinates available

for each sample, just the points entered and the approximate area in relation to the other points. This is probably possible to correct with the right software.

When choosing the samples, there was no way to tell with the naked eye which rocks would contain the largest fluid inclusions, or in which parts. Therefore, it is possible that the rock samples that were discarded would have given a better understanding of the fluid inclusions than the ones that were chosen. This is something that one cannot determine in any other way than preparing all of the sample for PTS, but this is both expensive and time-consuming for both the preparation lab and the student.

For the microscopic analysis, most of the effort was put towards finding nice fluid inclusions and not very much on the petrography itself. This could mean that some minerals might have been overlooked or been mistakenly characterized as another mineral. This is regrettable, but will hopefully not affect the final results very much.

In the SEM-CL, most of the markings on the sections were wiped off while cleaning the carbon off, a slight polish is also often performed on the surface, so that the areas imaged could be difficult to find for further investigations. When the FS were analyzed, the area processed was merely 1 x 1 mm, and for two of the samples it was not possible to rediscover with certainty where the images were taken. This could have been avoided by marking the samples better, and photographing them with the markings on to compare with the cleaned sample after SEM-CL.

For the microthermometry, a lot of operator-, hardware- and software errors have occurred. Starting with operator errors, it is likely that the temperatures have not been recorded perfectly within 0.1$^{\circ}$C, due to failure to observe correctly, and slow reaction while stopping the temperature controller. Sometimes, limitations in the human eye and/or the hardware (microscope resolution) may have hindered observations of, for instance, first melting of clathrates and/or ice. This leads to less than perfect results, and further difficulties analyzing the fluid inclusions to reveal their exact properties.

Another error has been failure to volumetrically measure all of the fluid inclusions before partaking in any heating experiments. This has inevitably led to decrepitation of the fluid inclusions, meaning that the liquids and vapor has had an uncontrolled expansion in volume, and it will not be possible to properly measure it. In return, it will not be possible to calculate the bulk properties of the inclusion.  This has been a perfect example of a rookie mistake,

which can probably be avoided by thinking the experiment through a couple of extra times, and/or asking for experienced advice or supervision.

Additionally, when making approximations for the liquid/vapor ratio, it was assumed that the ratio of the areas would be a good approximation for the ratio of the volumes. This is probably not the case, but when trying the other approximation explained under Chapter 3.5, the estimated volume ratio was less than 1% vapor, more than 99% liquid for $H_2O$-rich inclusions, and up to 5% for very $CO_2$ -rich inclusions, which seemed very unlikely.

It is not clear whether hardware or software errors were the cause of one particular problem, but after about a week, the Linkam stage used a very long time to cool the samples down to a proper -190˚C. In the beginning, cooling down from room temperature to -190˚C by liquid nitrogen took about 10 minutes in total, but after a while it took at one time as much as 45 minutes to get the sample cooled properly. It would be rather fast down to approximately -110˚C, but would then decrease gradually in cooling speed down to -145˚C, and drastically towards -190˚C. Because of this, some of the inclusions have been cooled only until the point of -150˚C.

Another effect of this problem was that there was simply not enough time to do all of the planned experiments. This has led to a drastic reduction in number of experiments, where the goal was between 200 and 250 inclusions fully measured, just over 40 have been properly investigated. Around 150 inclusions have been studied in one way or another.

Seeking other Linkam Stages in Norway to replace the faulty, current one was attempted, but unfortunately, the only one found was in Oslo, and was set up so specifically that it was requested that it would not be utilized for these experiments. There were also some attempts at repairing the current one, by changing the tube from the liquid nitrogen-container and changing into “fresh” liquid nitrogen, but neither had any effect. Additional repairs were not attempted due to time limitations.

# Theory

## 4.1 Magmatic-hydrothermal ore-forming processes

### 4.1.1 Introduction

The interaction between magmatic and hydrothermal processes is very important for the forming of several ore types. Most of the ore occurrences are formed by hot fluids interacting with or altering the minerals in the crust. The most primitive fluids are derived from magmas that are cooled and crystallized, but meteoric water and sea water can also play an important role (Robb, 2005).

### 4.1.2 Water and granite

The water found in granitic melts is mostly extracted from the minerals in the crust that also comprise the magma itself. The melting of a biotite- or biotite and hornblende-bearing source rock will result in a metaluminous I-type granite. These granites are relatively "dry" compared to peraluminous S-type granites, derived from the melts of a muscovite- or muscovite and biotite-bearing source rock. The dry I-type granites are the ones most often related to porphyry-Mo-Cu-occurrences. Due to the different source rocks required to form I- and S-type granites, the water content of the granites will partly be a function of these minerals, and partly by pressure- and temperature conditions (Robb, 2005).

When a granitic magma crystallizes, the remaining fluid phase will be dominated by anhydrous minerals, and the concentration of incompatible elements such as water and other volatiles will increase. At some point during the crystallization, the granitic melt will be saturated with water, and the water will assume its own, distinct phase. This process is called "boiling", even though it doesn't necessarily have anything to do with the fluid – vapor – transition. The water phase will usually rise and become concentrated in the roof of the chamber due to density differences, the water phase having a density of around 1 g/cm$^3$ versus the more heavy, granitic magma at approximately 2,5 g/cm$^3$ (Robb, 2005).

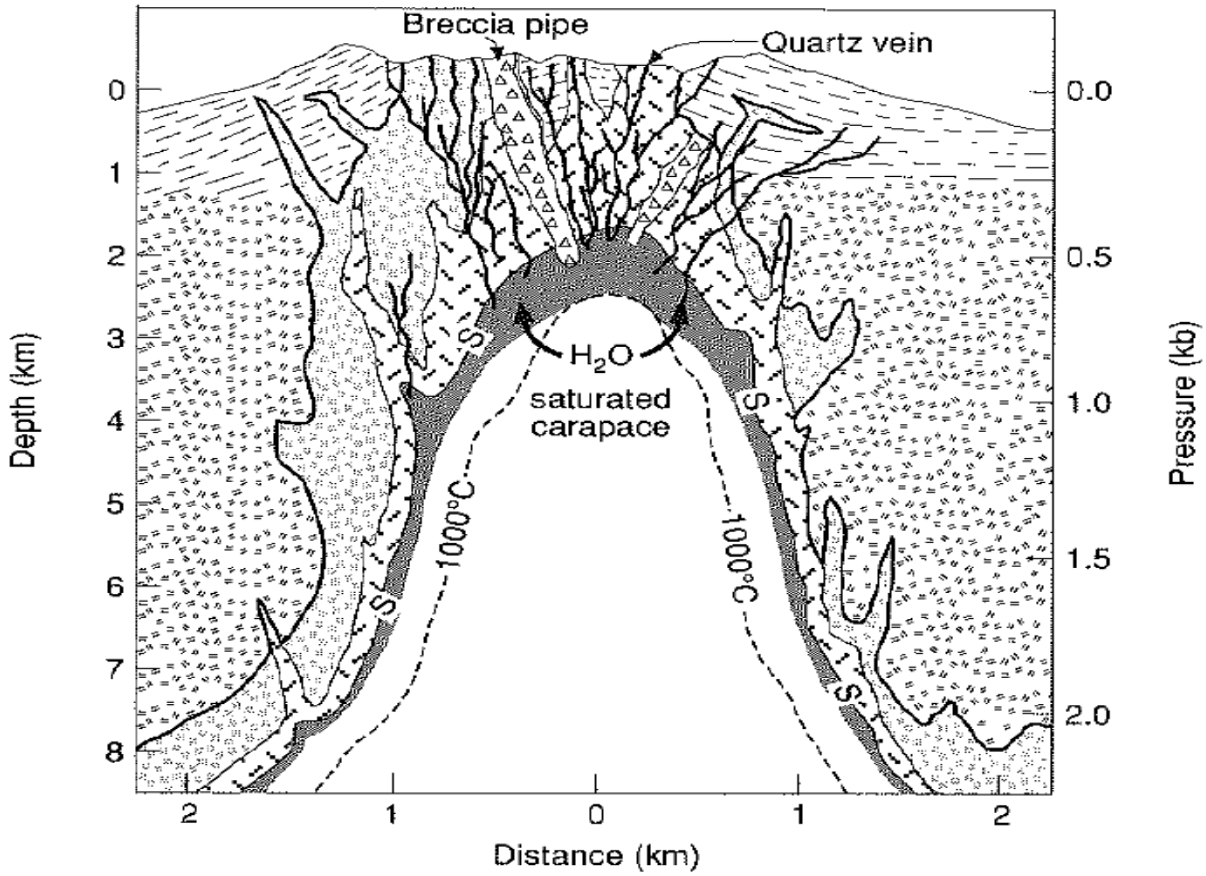


**Figure 6: Progressive crystallization from Burnham, 1967 (Robb, 2006)**

Figure 6 shows progressive crystallization in a high-level granodioritic intrusion. The S shows the hypothetical position of the $H_2O$-saturated granite, and the gray area shows where aqueous fluid saturation will occur in the residual magma. The original melt for this model contains approximately 2.7 mass% $H_2O$. When approximately 10% of the magma is crystallized, the $H_2O$ saturation is already reached by first boiling with the residual melt containing 3,3 mass% of water. (Robb, 2005)

### 4.1.3 First and second boiling

In high-sitting systems with relatively low temperatures and pressures, such as the one displayed in Figure 6, water saturation will usually happen as a first boiling. The magma chamber may crack and relieve the pressure, thereby precipitating water as a separate phase, or first boiling may occur due to the upward emplacement of the water saturation. At low pressures (>2kb), the fluid will actually boil because the gas pressure equilibrium is as large as the overlying pressure on the magmatic system, and volatile gases will vesiculate ("boil").

In lower-sitting systems, the water saturation will first occur after extensive crystallization of the anhydrous minerals under isobaric conditions (conditions with constant pressure). The

water saturation happens because the volatile content of the melt will exceed the saturation point, giving a second boiling.

First and second boiling is dependent and independent of pressure changes in the chamber, respectively. In addition, the water saturation itself is dependent of the original water content of the melt. A melt with a high volatile content will saturate at an earlier phase in the crystallization than a melt with a low volatile content (Robb, 2005).

Enriching a volatile fluid in metals will require the fluid to circulate in and around the intrusive complex it's derived from, rather than to just rise to the roof zone of the chamber at the point of saturation. This will be possible due to the mechanical energy the watery fluid will release to the surroundings. The volume of the silicate melt and the volume of the low-density watery fluid will be larger than the same amount of water-saturated magma. This may lead to an overpressure in the chamber, giving a brittle deformation of the chamber in the form of cracking. These hydrofractures usually have a rather steep dip, as the rocks will expand in the direction of least principal stress and this often means the horizontal plane. The hydrofractures will start in the zones of fluid formation and will rise to the granite roof zone, and will sometimes continue into surrounding rocks and through to the surface. The experimental works of Dingwell, Holtz & Behrens (1997) confirms that this scenario is likely if the granite is set high in the crust, as brittle fracturing may occur both in the intrusions and in the surrounding rocks, allowing the ore-bearing, aqueous fluids to circulate in these cracks (Robb, 2005).

### 4.1.4 Quartz veins and fluid compositions

Quartz may precipitate from hot watery solutions into cracks in the crust. Water is a powerful solvent, and this property increases with increasing pressure and temperature, allowing it to dissolve considerable amounts of most rock-forming minerals. As a solute, silica takes the form of $H_4SiO_4$, and with this being a typical constituent of hydrothermal solutions, quartz is often found in veins. The solution properties of quartz in water are not only dependent of pressure and temperature, but also pH and salinity (Robb, 2005).

In an experiment done by Burnham (1967) where granite and pure water was allowed to react under a range of pressure- and temperature conditions, it was proven that at high temperature and pressure (10 kbar and 650˚C), the water could dissolve up to 9 mass% of granite, and the Si, Na and K content was approximately equal in proportions as the composition of eutectic granite. With decreasing pressure and temperature the solubility of all three elements sank,

but Na and K also decreased relative to the Si. This is an explanation of why quartz is the main mineral dissolved near the surface (Robb, 2005).

### 4.1.5 Other important incompatible elements

$CO_2$ is quite often found in large quantities along with magmatic fluids, and the solubility of it increases by the alkalinity and increasing pressure of the magma. The solubility of $CO_2$ is a lot less than the solubility of $H_2O$, meaning that the $CO_2$ will separate into its own phase early in the solidification process. From this follows that early formed vapors will contain more $CO_2$ than later formed ones, and it is presumed that a magma may be saturated by $CO_2$ as far down as mid-crust. Volatiles formed in systems that have undergone severe differentiation or is situated high in the crust will be $H_2O$-dominated as the $CO_2$ and other relatively insoluble gases will have boiled (Robb, 2005).

The $CO_2$ content is not directly involved in the transport and concentration of metals in hydrothermal fluids, but is rather important for the distribution and precipitation of metals. $CO_2$ in a watery fluid will increase the immiscibility between gases and saline fluids, thus increasing the precipitation of metals from the solution. Immiscibility is the segregation of a low pressured brine into a dense, high-saline brine and a less dense, low saline watery solution. In addition, effervescense can give certain types of metamorphosis in the host rock and increase the pH in the remaining fluids so that the ore-forming processes will be further influenced (Robb, 2005).

The sulphur content in magmatic fluids is usually low, this might be due to the $SO_2$ partitioning into the vapor phase when boiling. The oxidized and reduced forms of sulphur are mutually exclusive, meaning they will either exist as a $SO_2^{2-}$ complex or as a $HS^-$ complex. The magmatic fluids associated with I-type granites are fairly oxidized, thus containing $SO_2^{2-}$. This fractionates into the watery, fluid phase, and porphyry-Mo-Cu-ores are related to large quantities of sulphides in the forms of pyrite and chalcopyrite. In reducing S-type granites, aqueous fluids with a lower $H_2S$ or $HS^-$ concentration are separated, and these fluids keep the sulphide minerals stable through to lower temperatures, assisting the formation of $Sn^-$ and $W^-$ oxides relatively early in the mineralization sequence (Robb, 2005).

### 4.1.6 Partitioning of Cu and Mo

Candela and Holland (1984) measured the partitioning of Cu and Mo between a granitic melt and an aqueous fluid containing $F^-$ and $Cl^-$ experimentally at 750˚C and 1,4 kbar. The experiment clearly showed that Cu is strongly controlled by the concentration of Cl in the

aqueous phase, while Mo is not affected. Even though Mo will partition into the aqueous fluid, the partition coefficient is constant and stays constant regardless of the concentration of $Cl^-$. Neither Cu or Mo are affected by the F- content of the aqueous fluid. This might be explained by fluorine's habit of partitioning into the silicate melt, thus not being present as a complex agent in the fluid phase (Robb, 2005).

## 4.2 Formation models for porphyry Cu- and Mo- deposits

### 3.7.1 Introduction

Porphyry deposits are the most important sources of Cu and Mo on a worldly basis, and these are associated with oxidized I-type granites formed by the melting of subducted oceanic crust. The porphyry deposits are usually separated into two types, Cu-(Mo) where Cu is the dominant metal with some Mo and Au, and Mo-(Cu), where Mo is the dominant metal along with some Cu and W. A concept sketch of these two types of deposits can be found in Figure 7 (Robb, 2005).

### 3.7.2 The formation of a Cu-(Mo) porphyry deposit

A Cu-(Mo) porphyry deposit is the product of a melt with low water content, rising high up in the crust before significant crystallization can take place. Some might even extrude and crystallize on the surface. Seeing as there won't be much overlying load on the magma chamber, water saturation will happen early in the crystallization process, and the water content will not be significantly higher than the initial melt. This deposit type is represented as number 1 in Figure 7 (Robb, 2005).

Cu is a compatible element in the granitic melt and especially in sulphides and biotite, but as the water saturation is reached very early in the crystallization process, very little Cu will have managed to crystallize with these. The brine will have a high concentration of Cl-, and can easily be enriched in Cu because of this.

Mo is an incompatible element in a crystallizing, granitic melt, but it will not enrich a lot before water saturation is reached because the crystallization hasn't progressed much at this point. At the point of water saturation, Mo will partition into the aqueous fluid phase, but seeing as it's partition coefficient is rather small, and also unaffected by the Cl- concentration, Mo will never reach considerable concentrations in the fluid phase. This means that a highly lying, granodioritic I-type melt will exsolve an aqueous fluid phase very enriched in Cu, but only moderately in Mo (Robb, 2005).

### 3.7.3 The formation of a Mo-(Cu) porphyry deposit

To form a Mo-(Cu) deposit it will be necessary for the I-type magma to have a slightly higher water content than the dry magma needed for the deposition of a Cu-(Mo) porphyry, and it should not rise as high in the crust, as shown in Figure 7. Given this, there will be a higher concentration of water due to the more crystallized chamber at the time of water saturation.

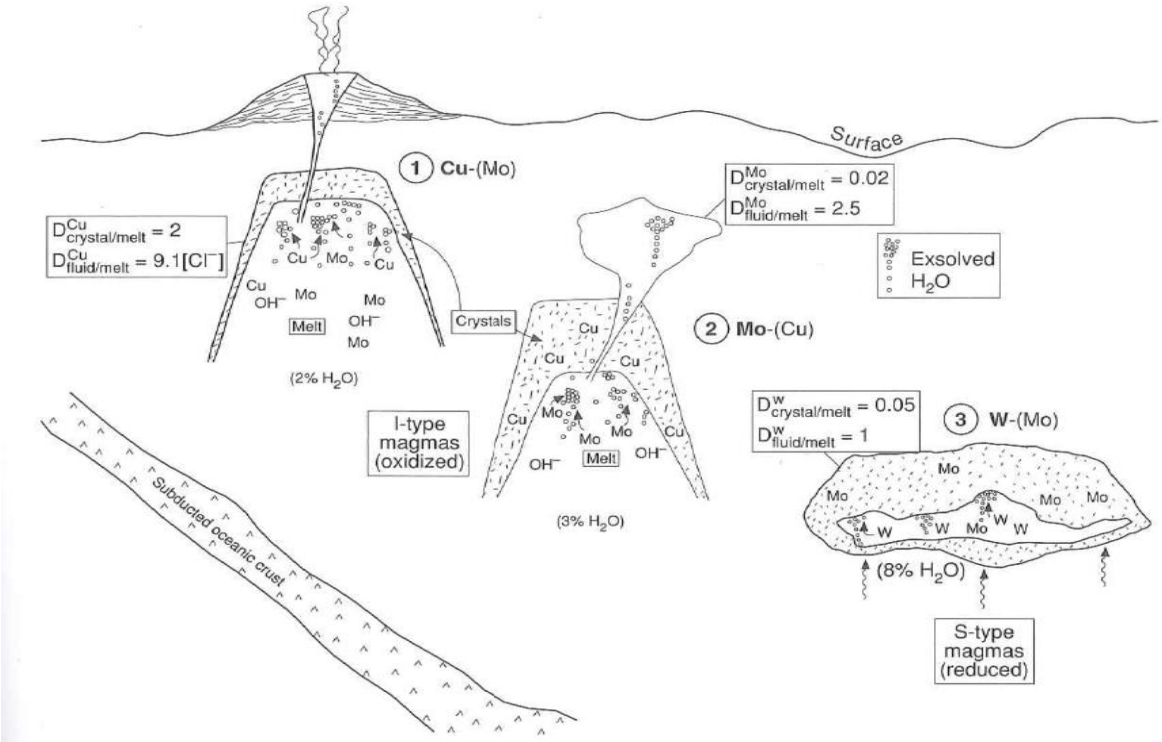


**Figure 7: Model for the origin and formation of porphyry type deposits (Robb, 2005)**

As the magma crystallizes, the Cu will crystallize along with it, and form the marginal zones of the chamber.

Mo is, as previously mentioned, incompatible, and will continue to enrich in the residual melt. At the time of water saturation, Mo will concentrate even more into the aqueous fluid phase due to the partition coefficient. The aqueous fluid phase will not be particularly enriched in Cu despite its high salinity, as the Cu content is depleted because of the earlier crystallization. (Robb, 2005)

### 4.2.4 Climax-type Porphyry Molybdenum Deposits

Climax-type porphyry molybdenum deposits are very rare, with possibly as few as 13 documented deposits on Earth, and are mainly found in North America. Their locations can be found in Figure 8. The deposits are made up of stockwork quartz-molybdenite veins that lie

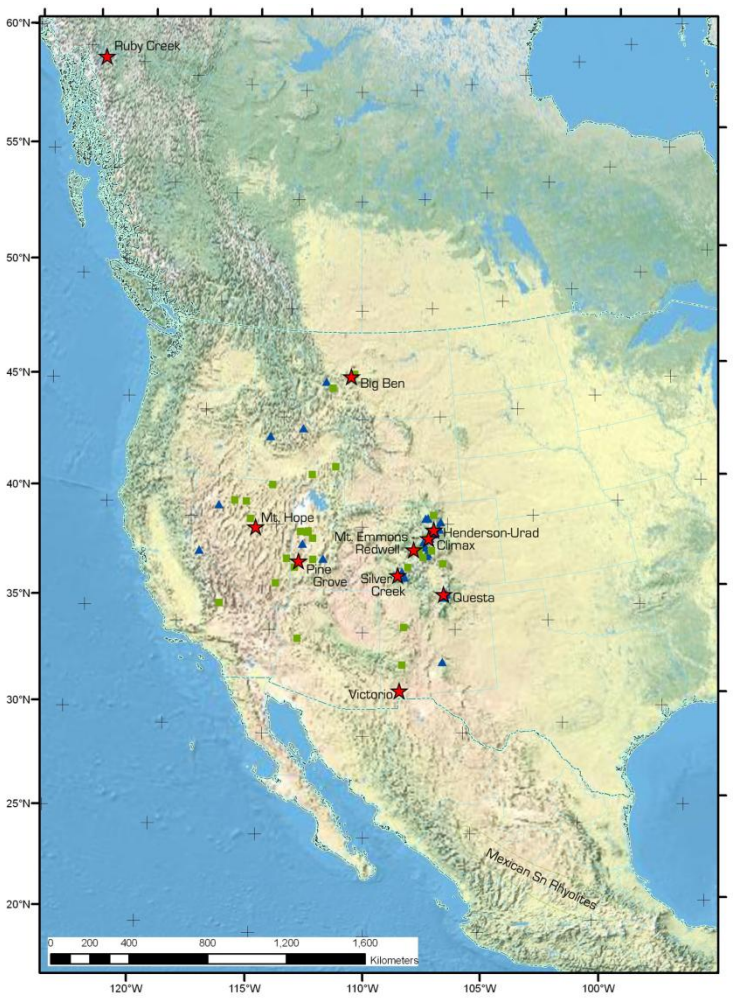


**Figure 8: Location of Climax-type porphyry molybdenum deposits, prospects, and igneous centers with Climax-like compositions. The red stars show the deposits, the blue triangles show the prospects and the green squares show the igneous centers (Ludington & Plumlee, 2009).**

above and around porphyry bodies made up of highly evolved calc-alcaline granites and subvolcanic rhyolites. The porphyric plutons are formed in and extensional environment in the continental crust, and formed after peak activity of a magmatic cycle in the middle to late Cenozoic (Ludington & Plumlee, 2009)
Climax-type deposits are related to some of the alkaline A-type granites found within continental rifts in Norway and Greenland. They can be viewed as a special case of pluton-related deposits associated with rare-metal granites, where the rare metals are found in uncommonly high concentrations of normally dispersed elements such as Fl, Li, Rb, Cs, Sn, Ta, Nb and Mo (Ludington & Plumlee, 2009).

Molybdenum is almost always found as molybdenite ($MoS_2$) in the Climax-type deposits, and is the primary commodity. The Henderson and Questa mines only produce molybdenum, while Climax also has recovered some wolframite, cassiterite and monazite. No other Climax-type deposit has been mined yet (Ludington & Plumlee, 2009).

### 4.2.5 The Questa Porphyry Mo deposit, USA

The Questa porphyry molybdenum deposit is hosted in the Late Oligocene Questa Caldera located in the Latir volcanic field, which started the formation of stratovolcanoes and lava domes around 28 Ma. The caldera itself formed at around 25.7 ± 0.1 Ma when more than 500 $km^3$ of pyroclastic rocks were ejected, and granitic and rhyolitic intrusions were formed in the north and center of the caldera within the next 1 Ma. The last magmatic activity in the region happened to the south, outside of the caldera margin, giving a distinct north to south younging of the intrusion ages. The molybdenum mineralization is restricted to some intrusions of magmatic-hydrothermal breccias (MHBX) in the south (Klemm, Pettke, & Heinrich, 2008).

The lowest part of the MHBX is made up of an igneous breccia with aplite matrix, where the clasts are angular, biotite-altered andesite and occasionally grey rhyolite porphyry. The igneous breccia matrix grades upwards into zones of hydrothermal breccia matrix, and the transitional zone between them has minor amounts of molybdenite in an aplitic matrix. The upper part of the breccias is made up of a hydrothermal breccia containing quartz, phlogopite and molybdenite, and in some zones the phlogopite and quartz crystals are overgrown with the molybdenite. The molybdenite is again overgrown by anhydrite, apatite and calcite. Stockwork veins consisting of quartz, fluorite, molybdenite and anhydrite cut the MHBX, and the molybdenite is intergrown with quartz (Klemm, Pettke, & Heinrich, 2008).

## 3.8 Fluid inclusions

### 3.8.1 Introduction

Fluid inclusions can be found in almost all rock types, but are most common in crustal rocks. They usually represent paleo-fluids, but may also have originated more recently. The information that might be obtained from fluid inclusions is the fluid composition, fluid density, pressure - and temperature conditions at the time of formation, and the development of the rocks/fluids over time (Bakker, 2011).

The fluid composition may be obtained as elements, dissolved ions and molecules, stable isotopes and radiogenic isotopes. The temperature of homogenization is directly correlated to the composition of the fluid. The fluid density of the paleo-fluids may only be measured by measuring fluid inclusions (Bakker, 2011).

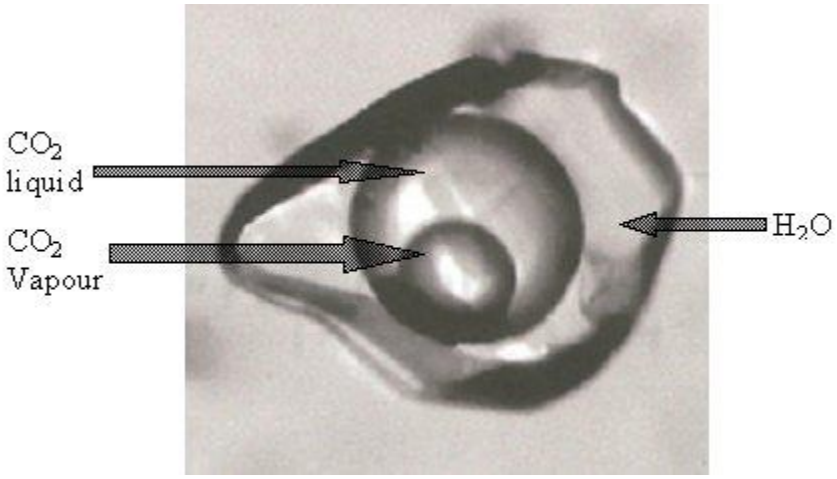


**Figure 9: Fluid inclusion in detail. L1, L2, V (Geological Survey of India)**

The pressure – and temperature conditions at the time of formation are found by obtaining the temperature of homogenization, as it will provide the minimum value of the formation temperature. In normal conditions, by homogenous entrapment, the formation conditions may be found by the minimum temperature and – pressure. This will be found on an isochore, somewhere in the P-T-room.

The development of the rocks and fluids over time can be known a bit better by comparing several generations of fluid inclusions. The interpretation of fluid composition, density and P-T-conditions for the different generations may provide information about the deformation history of the system (Bakker, 2011).

### 3.8.2 Important parameters

Eutectic temperature, $T_e$, is the minimum temperature of fluid stability, which means that it's the temperature where one solid phase disappears and a fluid phase is formed at the same time. The eutectic temperature may indicate a specific system, for a binary system of H2O – NaCl, $T_e$ = -21˚C. This transition may be difficult to observe optically.

The nucleation temperature, $T_n$, can be measured by cooling experiments (microthermometry), when a brine nucleates a salt crystal. This is also indicative of the salinity of the system, a low $T_n$ indicates a high salinity.

The homogenization temperature, $T_m$, is found when two phases homogenizes into one. This may be a liquid- and vapor-phase fluid inclusion homogenizing either into the liquid or the vapor phase (Bakker, 2011).

The decrepitation temperature, $T_d$, is the temperature where the internal pressure of the fluid inclusions exceeds the external pressure of the rock, making the rock crack around the inclusion. The fluid inclusions are thereby exposed to an uncontrolled increase of volume, and if the cracks reaches out through the crystal it may lead to leaking of fluids from the inclusion. $T_d$ is controlled by the size and shape of the inclusion.

Studies of fluid inclusions in Cu-Mo-porphyry systems show that the earliest generation of fluids to be trapped in primary inclusions often have had high temperatures and salinities. This has been showed with fluid/gas separation and daughter crystals in the inclusions. Usually the daughter crystals are made of halite (NaCl), or sometimes sylvite (KCl). LA-ICP-MS analyses have proved that the fluids in the inclusions also may contain considerable amounts of Fe, Mn, Cu, Pb and Zn. (Bakker, 2011)

Fluid inclusions are generally multiphase when examined at room temperature, and the two most common phases are vapor and liquid. An example of a multiphase vapor-liquid inclusion can be found in Figure 9. Sorby (1858) explained that this phase separation is due to differential shrinkage when the crystal around and the fluid within the inclusion cooled, and that this could be reversed if the inclusion was heated. This means that every fluid inclusion is a geothermometer, that may divulge the temperature of the different geologic events the rock has been through (Bakker, 2011).

The two most misunderstood areas of fluid inclusion studies are, according to Roedder and Bodnar (1980), the effect of the hydrostatic pressure during the formation of the crystal and

its influence on the thermometric results, and how to make the best estimate of this pressure with the help of the inclusion data.

When working with geothermometry, the following assumptions must be made according to Roedder and Bodnar (1980):

1. The fluid was homogenous at the time of entrapment
2. The cavity where the fluid is trapped have not changed in volume after sealing
3. Nothing goes in to or comes out of the inclusion after sealing
4. The effect of the pressure is unknown, or insignicficant
5. The source of the inclusion is known

The first assumption is essential for geothermometry, but the entrapment of a heterogenous mixture of two fluid phases, especially liquid and vapor, may give an excellent geobarometer.

The second assumption usually doesn't matter much, as the most common volume change happens as the cooling makes the fluid precipitate on the walls of the inclusion. This will be reversed during heating. The volume of the inclusion will be larger at the homogenization temperature $T_m$ in the laboratory than it was at the time of formation, as the host mineral expands when brought to the surface. The volume of the inclusion will increase with 0.1% per kbar of decreasing pressure due to the compressibility. This effect is quite a lot lower than the margins of error from other sources, and may generally be ignored (Roedder & Bodnar, 1980).

The third assumption is made due to some hydrogen diffunding from the inclusion and into the host mineral, and assuming also that the hydrogen comes from H2O, the rest (resterende) o2 may oxidize the components of the fluid. This could make a sulphide into a sulphate, or O2 may diffund into the host mineral as $H^+$ did. The volume changes here will be hard to estimate.

The fourth assumption is based on the homogenization of a vapor and a liquid in an inclusion only giving a minimum value of $T_t$. All inclusions of a given composition "trapped" along an isochore will homogenize similarly, so that either P or T have to be known to find the other.

The fifth assumption is creating problems in many inclusion studies. The inclusions in a crystal has generally been trapped under more than one phase of the growth, fracturing and healing of the crystal. Because of this, the source of the inclusion and the order of formation

may be interpreted in different ways, but this is usually of no consequence to geobarometers. (Roedder & Bodnar, 1980)

### 4.3.3 Fluid inclusions in the Questa porphyry Mo deposit

The igneous and the transitional parts of the MHBX only contain very small fluid inclusions that are poorly preserved. Larger inclusions usually showed decrepitation features, such as halos of smaller inclusions around larger ones, or irregular, flat shapes. Rock deformation appears to have destroyed the majority of the larger inclusions (> 10µm). The best preserved fluid inclusions were found in the hydrothermal part of the MHBX, where the quartz was protected by molybdenite from later deformation (Klemm, Pettke, & Heinrich, 2008).

In the deeper, igneous part of the MHBX, only fluid inclusions smaller than 15µm were found. These inclusions were two-phased, liquid and vapor, without any daughter crystals, and showed highly variable microthermometric behavior. The final ice melting occurred between 0.5°C and -4.3°C, and the final clathrate melting occurred from about 6°C to 9.3°C. These measurements gives salinities for the inclusions between 1 and 7.5 wt% $NaCl_{equiv}$. The vapor size at room temperature occupied between 40 and 60% of the volume, so the homogenization temperature was not determined (Klemm, Pettke, & Heinrich, 2008).

In the upper, hydrothermal parts of the MHBX, SEM-CL reveals three generations of quartz, where the oldest generation (hereafter named $Q1_{MHBX}$) appears light grey and unzoned. The $Q1_{MHBX}$ often hosts clusters of intermediate-density inclusions of possibly primary origin. The $Q1_{MHBX}$ is overgrown by $Q2_{MHBX}$, an idiomorphically growth-zoned quartz, which also fills secondary cracks in $Q1_{MHBX}$ and contains inclusions of brine ($B_{MHBX}$) and vapour ($V_{MHBX}$). The youngest quartz generation, $Q3_{MHBX}$ , occurs as thin SEM-CL black overgrowths, crack fillings and spots interpreted to represent decrepitated fluid inclusions, mainly in the $Q1_{MHBX}$. Molybdenite inclusions were observed in other crystals in the same samples, lining the contact between $Q2_{MHBX}$ and $Q3_{MHBX}$ (Klemm, Pettke, & Heinrich, 2008).

### 3.8.3 Determining salinity in fluid inclusions

**Table 2: Melting temperatures of ice in a $H_2O$-NaCl system determining salinity. From Bodnar, 1993 in (Bakker, 2011)**

Final melting temperature of ice, in the presence of a vapour and liquid

| Tm | .0 | .1 | .2 | .3 | .4 | .5 | .6 | .7 | .8 | .9 |
|---|---|---|---|---|---|---|---|---|---|---|
| **-0.** | 0.00 | 0.18 | 0.35 | 0.53 | 0.71 | 0.88 | 1.05 | 1.23 | 1.40 | 1.57 |
| **-1.** | 1.74 | 1.91 | 2.07 | 2.24 | 2.41 | 2.57 | 2.74 | 2.90 | 3.06 | 3.23 |
| **-2.** | 3.39 | 3.55 | 3.71 | 3.87 | 4.03 | 4.18 | 4.34 | 4.49 | 4.65 | 4.80 |
| **-3.** | 4.96 | 5.11 | 5.26 | 5.41 | 5.56 | 5.71 | 5.86 | 6.01 | 6.16 | 6.30 |
| **-4.** | 6.45 | 6.59 | 6.74 | 6.88 | 7.02 | 7.17 | 7.31 | 7.45 | 7.59 | 7.73 |
| **-5.** | 7.86 | 8.00 | 8.14 | 8.28 | 8.41 | 8.55 | 8.68 | 8.81 | 8.95 | 9.08 |
| **-6.** | 9.21 | 9.34 | 9.47 | 9.60 | 9.73 | 9.86 | 9.98 | 10.11 | 10.24 | 10.36 |
| **-7.** | 10.49 | 10.61 | 10.73 | 10.86 | 10.98 | 11.10 | 11.22 | 11.34 | 11.46 | 11.58 |
| **-8.** | 11.70 | 11.81 | 11.93 | 12.05 | 12.16 | 12.28 | 12.39 | 12.51 | 12.62 | 12.73 |
| **-9.** | 12.85 | 12.96 | 13.07 | 13.18 | 13.29 | 13.40 | 13.51 | 13.62 | 13.72 | 13.83 |
| **-10.** | 13.94 | 14.04 | 14.15 | 14.25 | 14.36 | 14.46 | 14.57 | 14.67 | 14.77 | 14.87 |
| **-11.** | 14.97 | 15.07 | 15.17 | 15.27 | 15.37 | 15.47 | 15.57 | 15.67 | 15.76 | 15.86 |
| **-12.** | 15.96 | 16.05 | 16.15 | 16.24 | 16.34 | 16.43 | 16.53 | 16.62 | 16.71 | 16.80 |
| **-13.** | 16.89 | 16.99 | 17.08 | 17.17 | 17.26 | 17.34 | 17.43 | 17.52 | 17.61 | 17.70 |
| **-14.** | 17.79 | 17.87 | 17.96 | 18.04 | 18.13 | 18.22 | 18.30 | 18.38 | 18.47 | 18.55 |
| **-15.** | 18.63 | 18.72 | 18.80 | 18.88 | 18.96 | 19.05 | 19.13 | 19.21 | 19.29 | 19.37 |
| **-16.** | 19.45 | 19.53 | 19.60 | 19.68 | 19.76 | 19.84 | 19.92 | 19.99 | 20.07 | 20.15 |
| **-17.** | 20.22 | 20.30 | 20.37 | 20.45 | 20.52 | 20.60 | 20.67 | 20.75 | 20.82 | 20.89 |
| **-18.** | 20.97 | 21.04 | 21.11 | 21.19 | 21.26 | 21.33 | 21.40 | 21.47 | 21.54 | 21.61 |
| **-19.** | 21.68 | 21.75 | 21.82 | 21.89 | 21.96 | 22.03 | 22.10 | 22.17 | 22.24 | 22.31 |
| **-20.** | 22.38 | 22.44 | 22.51 | 22.58 | 22.65 | 22.71 | 22.78 | 22.85 | 22.91 | 22.98 |
| **-21.** | 23.05 | 23.11 | 23.18 | | | | | | | |

Table 2 gives an easy to understand way of determining the salinity of fluid inclusions when in a $H_2O$-NaCl system. Put in the final melting temperature of ice and obtain the salinity directly (Bakker, 2011).

Table 3 devises the same principle to determine salinities by the dissolution of a NaCl-crystal present in the inclusion.

**Table 3: Melting of a halite crystal in a binary $H_2O$-NaCl system (Bakker, 2011).**

$H_2O$-NaCl fluid system

final melting temperature (or dissolution) of halite crystal

in the presence of vapour + liquid

| Tm | 0 | 100 | 200 | 300 | 400 | 500 | 600 | 700 | 800 |
|---|---|---|---|---|---|---|---|---|---|
| **0** | 26.31 *(0.0005)* | 27.75 *(0.075)* | 31.19 *(1.24)* | 37.74 *(6.24)* | 47.71 *(18.1)* | 60.58 *(32.6)* | 75.08 *(39.3)* | 89.10 *(28.2)* | 99.75 *(0.51)* |
| **10** | 26.41 *(0.0609)* | 27.98 *(0.11)* | 31.70 *(1.52)* | 38.59 *(7.05)* | 48.88 *(19.6)* | 61.99 *(33.8)* | 76.55 *(39.1)* | 90.37 *(26.0)* | |
| **20** | 26.52 *(0.0016)* | 28.23 *(0.15)* | 32.23 *(1.85)* | 39.47 *(7.93)* | 50.08 *(21.1)* | 63.41 *(34.9)* | 78.00 *(38.7)* | 91.61 *(23.7)* | |
| **30** | 26.63 *(0.0030)* | 28.51 *(0.20)* | 32.80 *(2.22)* | 40.38 *(8.99)* | 51.31 *(22.6)* | 64.84 *(36.0)* | 79.45 *(38.1)* | 92.80 *(21.1)* | |
| **40** | 26.75 *(0.0053)* | 28.81 *(0.27)* | 33.41 *(2.64)* | 41.33 *(10.1)* | 52.56 *(24.1)* | 66.29 *(36.9)* | 80.89 *(37.3)* | 93.95 *(18.4)* | |
| **50** | 26.88 *(0.0089)* | 29.13 *(0.35)* | 34.04 *(3.10)* | 42.31 *(11.3)* | 53.84 *(25.6)* | 67.74 *(37.6)* | 82.31 *(36.3)* | 95.06 *(15.6)* | |
| **60** | 27.02 *(0.014)* | 29.49 *(0.46)* | 34.71 *(3.61)* | 43.33 *(12.6)* | 55.15 *(27.1)* | 69.20 *(38.3)* | 83.72 *(35.1)* | 96.11 *(12.7)* | |
| **70** | 27.18 *(0.023)* | 29.87 *(0.60)* | 35.42 *(4.18)* | 44.37 *(13.9)* | 56.48 *(28.6)* | 70.67 *(38.8)* | 85.10 *(33.7)* | 97.11 *(9.69)* | |
| **80** | 27.35 *(0.035)* | 30.28 *(0.78)* | 36.16 *(4.81)* | 45.45 *(15.2)* | 57.83 *(30.0)* | 72.14 *(39.1)* | 86.46 *(32.1)* | 98.05 *(6.64)* | |
| **90** | 27.54 *(0.052)* | 30.72 *(0.99)* | 36.93 *(5.49)* | 46.56 *(16.7)* | 59.20 *(31.3)* | 73.61 *(39.3)* | 87.80 *(30.3)* | 98.93 *(3.56)* | |
| | mass% *(MPa)* | mass% *(MPa)* | mass% *(MPa)* | mass% *(MPa)* | mass% *(MPa)* | mass% *(MPa)* | mass% *(MPa)* | mass% *(MPa)* | mass% *(MPa)* |

Figure 10 shows a more intelligent way of displaying what's happening with the saline inclusion as it's heated. As the salinity increases, the melting temperature of the ice decreases, also as seen in Table 2, down to a salinity of 23,2 mass% where the temperature is -21.2°C. Above the triple point, hydrohalite is formed when the temperature increases, below ice forms (Bakker, 2011)

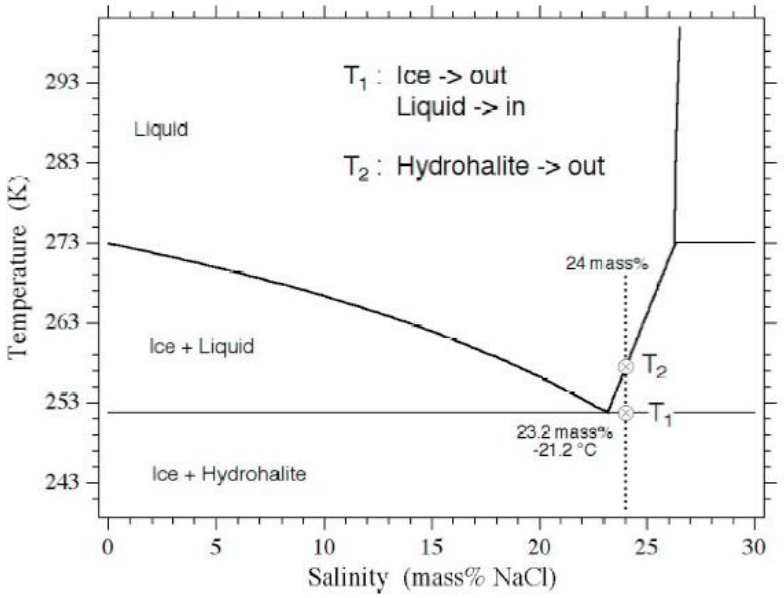


**Figure 10: $H_2O$-NaCl phase diagram (Bakker, 2011).**

# Results

## 5.1 Macroscopic analysis

The quartz veins in the roof of the granite are numerous and usually narrow, measured from two to 50 cm in width. They are found just at the top of the aplite part of the granite chamber, and are in places hard to keep track of because of their varying orientation, dip and resemblance to the aplite itself. The vegetation in the area is sparse, as seen in Figure 11, but would in places obscure the connections between the veins.

**Figure 11: Quartz vein resulting in sample 016 (S. Hagen, 2011)**

It is assumed that all of the quartz veins in the area were sampled at least once for this study. To find the connection between the veins, strike and dip-measurements were performed where possible, and the measurements were plotted in a stereo net. The strike and dip-measurements can be found in Table 4, and the stereonet in Figure 12. The strike and dip measurements were done by applying the right hand rule, which means that the strike is in the direction of the index finger, and the dip in the direction of the thumb of the right hand.

Table 4 shows the strike and dip measurements of the quartz veins.

| Sample | Strike | Dip | D.D | Sample | Strike | Dip | D.D |
|---|---|---|---|---|---|---|---|
| 001-1 | 341 | 50 | SW | 013-2 | | | |
| 001-2 | | | | 014-1 | 300 | 78 | |
| 001-3 | | | | 015-1 | | | |
| 001-4 | | | | 016-1 | | | |
| 002-1 | 210 | 70 | SE | 017-1 | 150 | 50 | NE |
| 003-1 | | | | 017-2 | | | |
| 003-2 | 335 | 45 | SW | 018-1 | 125 | 55 | NE |
| 004-1 | 205 | | SE | 019-1 | 242 | 68 | SE |
| 005-1 | | | | 020-1 | 250 | 80 | SE |
| 006-1 | 10 | 90 | NS | 021-1 | 20 | 54 | W |
| 006-2 | | | | 021-2 | | | |
| 007-1 | 160 | | NE | 021-3 | | | |
| 008-1 | 140 | 85 | NE | 022-1 | 230 | 70 | SE |
| 009-1 | 200 | | E | 022-2 | | | |
| 009-2 | | | | 022-3 | | | |
| 009-3 | | | | 023-1 | 98 | 54 | SW |
| 009-4 | 192 | 50 | E | 023-2 | | | |
| 010-1 | 192 | 50 | E | 024-1 | 150 | 78 | |
| 011-1 | | | | 025-1 | 212 | 82 | SE |
| 012-1 | 320 | 80 | | 026-1 | 115 | | N |
| 013-1 | 164 | 80 | E | | | | |

### 5.1.1 Orientation of the quartz veins

The results from the macroscopic analysis shows a variety of strike angles, varying all the way from 0 up to 359 degrees. There is a slight favor in the interval of 181 to 210 degrees, but since there are only 20 measurements in the field and not more than one measurement per sample due to difficult measuring conditions, not much can really be said about the direction of the quartz veins. What can be said is that in the field and from the measurements that were obtained, it seems likely that the quartz veins have no particular orientation. This means that the veins at the time of formation probably cross-cut the aplite both horizontally and vertically.

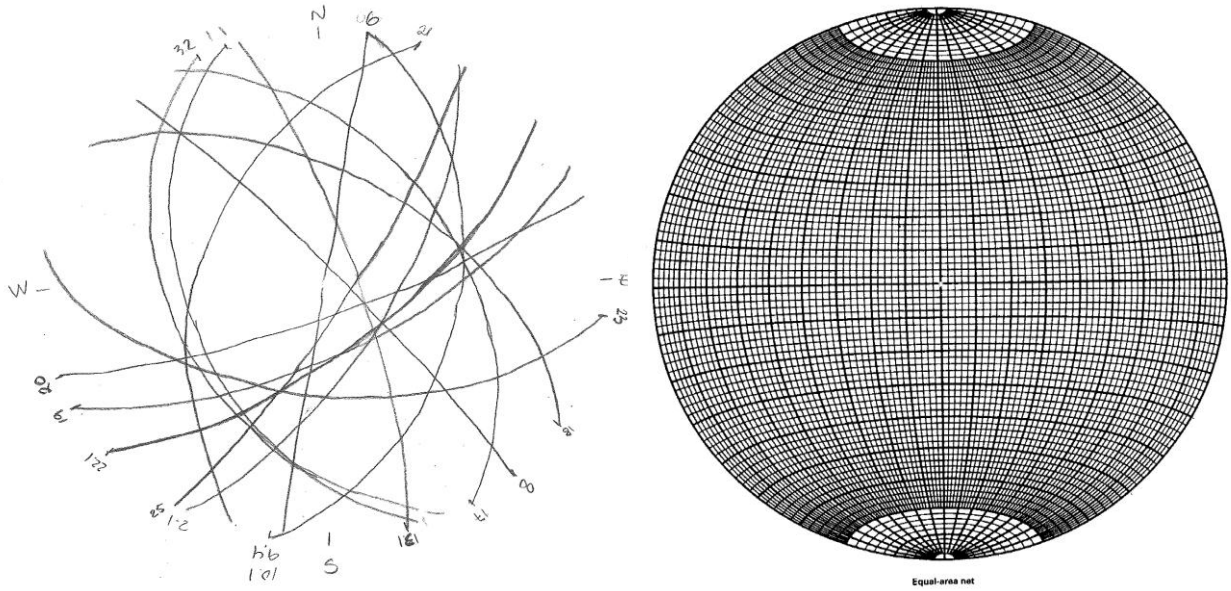


Figure 12: Left: Stereonet representation of Table 2. Right: Stereo net

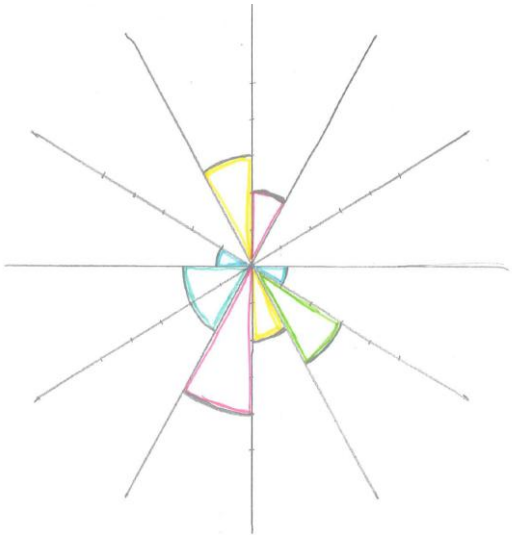

Figure 13: Measured strike directions by interval of 30 degrees. Dominant: 180-210 degrees.

### 5.1.2 Dip of the quartz veins

The dip angle is steep, more than 45 degrees up to vertical for all of the quartz veins measured. Based on that information only, one could assume that that meant that the quartz veins were deposited more or less horizontally in the chamber as it's seen from the side. But when the information about the orientation of the veins is taken into account, there is no way to determine any generalities about the quartz veins, apart from them being distributed completely randomly. When the results say that the dominant dip direction is towards the east, that is merely a function of the strike of the quartz veins being slightly in favor of a

southwards direction, as displayed in Figure 13.

## 3.9 Microscopic analysis

### 3.9.1 Introduction

17 of the 41 quartz vein samples were prepared into polished thin sections (PTS), and in addition two PTS from the aplite itself, collected by F. Jacamon (2006), were used for comparisons. The PTS were examined with an optical microscope to search for additional main elements and to search for fluid inclusions for further studies. The list of the samples and their preparation methods can be found in Chapter 3 Methods, Table 1.

The microscopic, visual impression of the quartz veins is that they are very similar in content, distribution and grain sizes. This indicates that there might have been a single quartz vein generation spreading out in random directions in the top of the chamber.

### 5.2.2 General description

The contents of the thin sections is quartz, altered feldspar and biotite mica, and the rock presents as heterogranular and holocrystalline with amoeboidal grain borders. The quartz is the most coarse-grained, followed by medium- to fine-grained feldspar, and lastly the fine-grained border-line accessory biotite.

### 5.2.3 Quartz

Quartz is naturally the most dominant mineral found in the thin sections, with a 90 - 100% share. The quartz grains are lightly zoned, and show pressure solution along the borders. The quartz is poikilitic in some grains, containing both feldspar and biotite to a larger or lesser degree. Figure 14 shows a thin section containing quartz and altered feldspar and is deemed a typical example of how the quartz appears. The quartz in the thin sections does not differ much from section to section, despite being collected over a rather large area. Some alterations in or near the grain boundaries have occurred. All of the fluid inclusions studied have been found in the quartz.

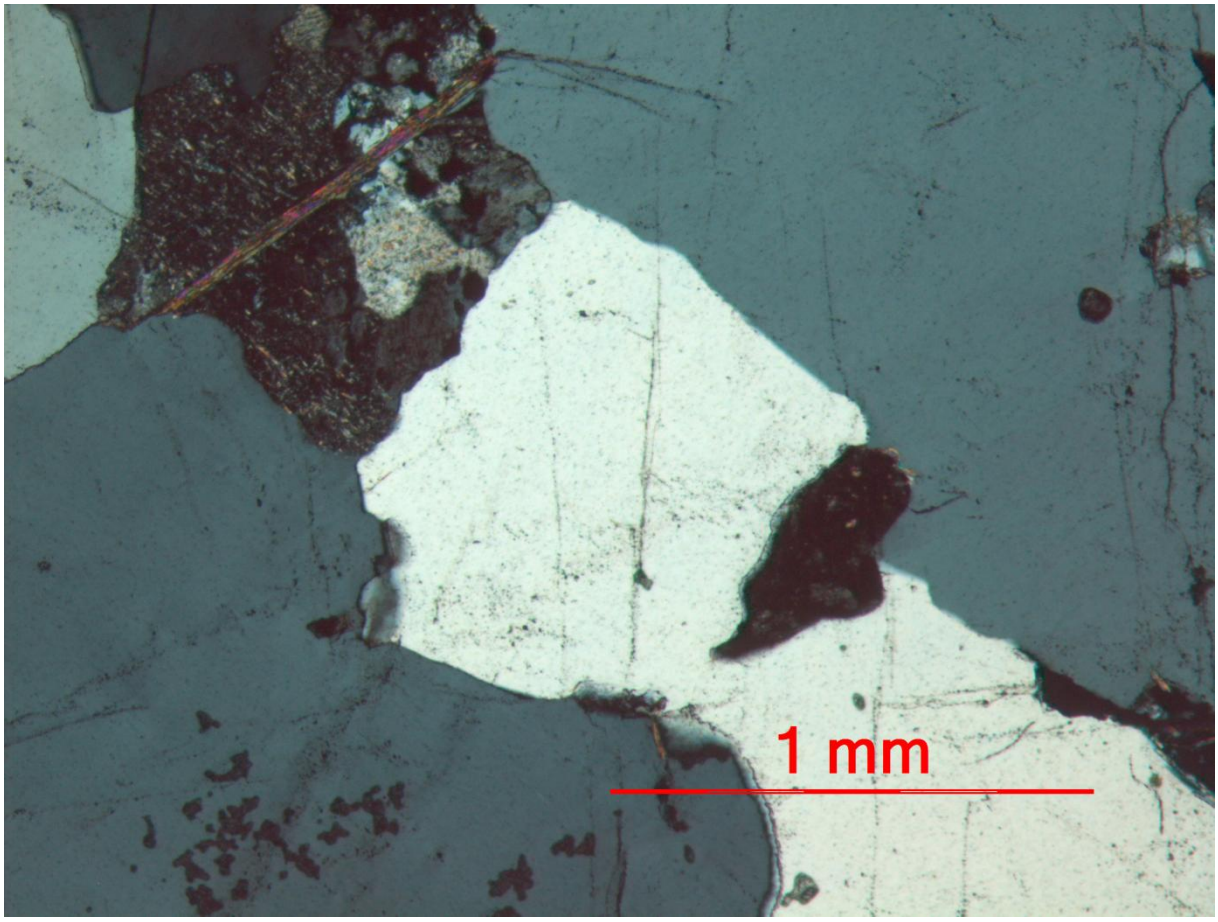


**Figure 14: Quartz, feldspar and sillimanite/mica from sample 16. Crossed polarizers. (S.Hagen, 2011)**

### 5.2.4 Feldspar

Feldspar is the second most common mineral found, with a share of about 3-10% where present. The feldspar is usually hydrothermally altered to sericite and/or saussurite, but can in some cases be distinguished due to the twin lamellae (albite, tartan and Carlsbad) present in the fresh or less altered parts of the feldspar. Due to the heavy alteration, there were no further attempts to classify the feldspar more thoroughly. A typical alteration of the feldspar is shown in Figure 15. Feldspar usually presents as amoeboidal grains of a medium size (0.1 – 5 mm along the longest axis), but does sometimes appear as fine grained particles within the quartz, and/or in aggregates with biotite.

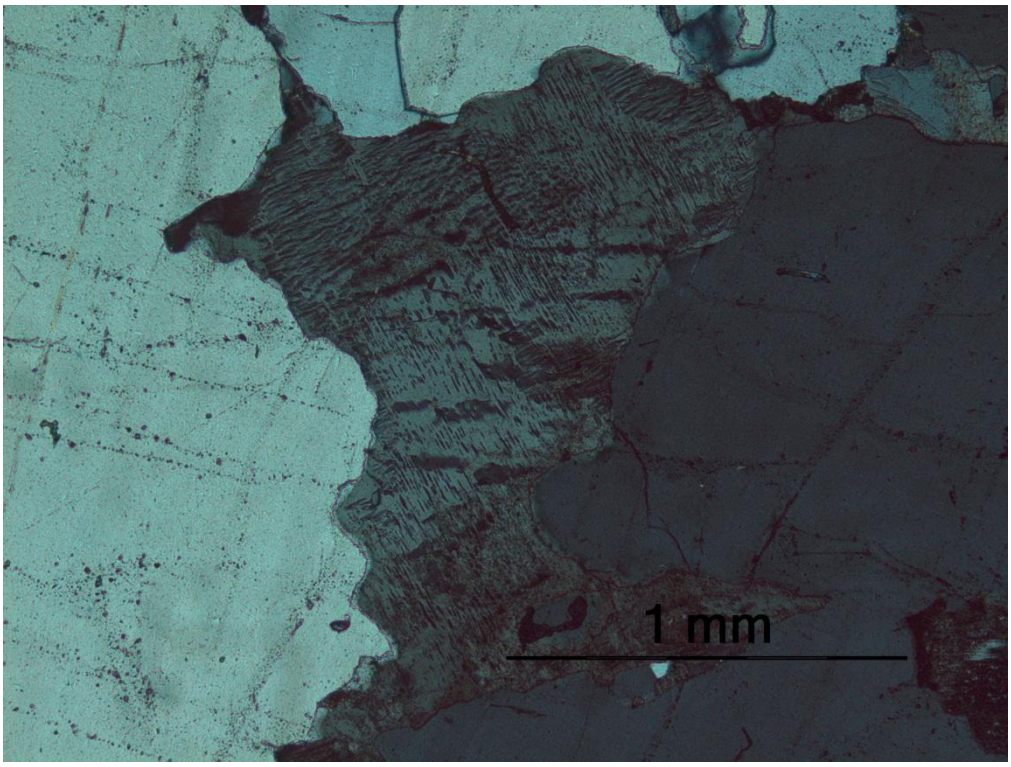


**Figure 15: Altered feldspar grain between two quartz grains. Some pressure solution along the grain borders. The dotted lines in the quartz grains are fluid inclusions. Crossed polarizers, optical microscope.**

### 5.2.5 Biotite

Biotite mica is an accessory mineral in the thin sections, and appears as fine grained lamellae or as infill in small cracks. In some thin sections the biotite is poikilitic, presenting as smaller grains within the quartz grains, and sometimes together with the feldspar, as in Figure 16. The biotite is not usually altered, but in some thin sections it presents as chlorite-like mica, meaning more fine-grained and light brown in color.

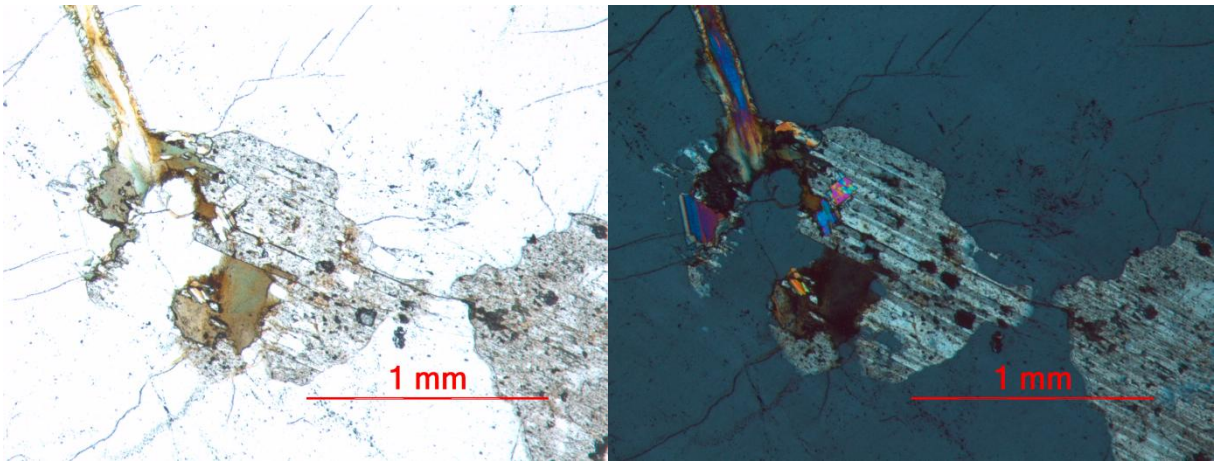


**Figure 16: Feldspar and biotite grains without and with crossed polarizers**

## 5.3 SEM-CL

### 5.3.1 Introduction

Two separate rounds of SEM-CL was performed, and on different samples. In the first round, the samples tested were PTS 003-2, 016, 024 and Apl-1B. Apl-1B is one of the PTS obtained from the works of Dr. F. Jacamon (2006) for his Ph.D-thesis.

From all the SEM-CL analyses the impression is that there is only one quartz generation per sample. By giving the images similar thresholds, one still obtains different colorations for some of the quartz, but generally they are found in the blue to green spectrum of 400 – 450 nm. The fluid inclusions cause recrystallization in their immediate surroundings, but do not change the general impression of the quartz.

In some of the images, a slight color change is apparent directly around the feldspars, in distances that are larger than the equipment's limit of detection. This implies that the feldspar alters the quartz slightly in their immediate surroundings, but in such a short range that it's not thought to affect the fluid inclusions. The fluid inclusions chosen for this study have not been within the range of this alteration, as the feldspars disturb the microscopic image slightly by being so altered.

### 5.3.2 SEM-CL

#### 5.3.2.1 003-2

PTS 003-2 shows an impression of a first generation quartz with secondary fluid inclusions. These are shown as reddish-black cracks in Figure 17. In the top right corner, the quartz seems a more light-blue colored. This is called variable luminescence, and is probably a cause of an unevenly distributed carbon coating.

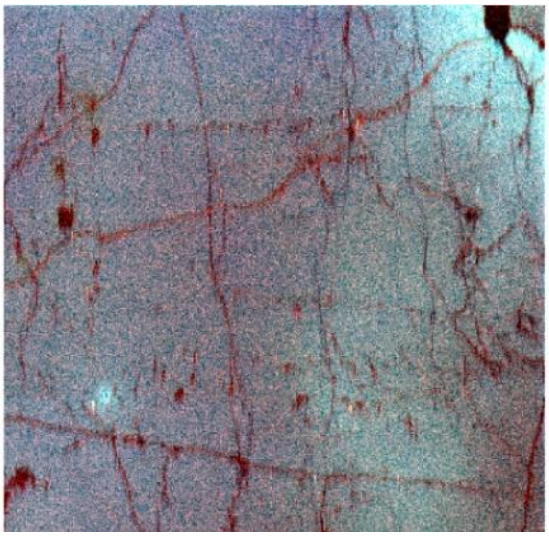

**Figure 17: SEM-CL image of thin section 003-2 (M. Raanes, S. Hagen, 2011)**

#### 5.3.2.2 016

PTS 016 is, like 003-2, very homogenous, as can be seen in Figure 18, indicating a simultaneous crystallization. The fluid inclusion cracks in this thin section are also secondary in nature, and apart from these, the quartz doesn't show any signs of a recrystallization. The red luminescence that is presenting as tiny dots throughout the quartz is probably due to primary fluid inclusions, which can cause very local recrystallization.

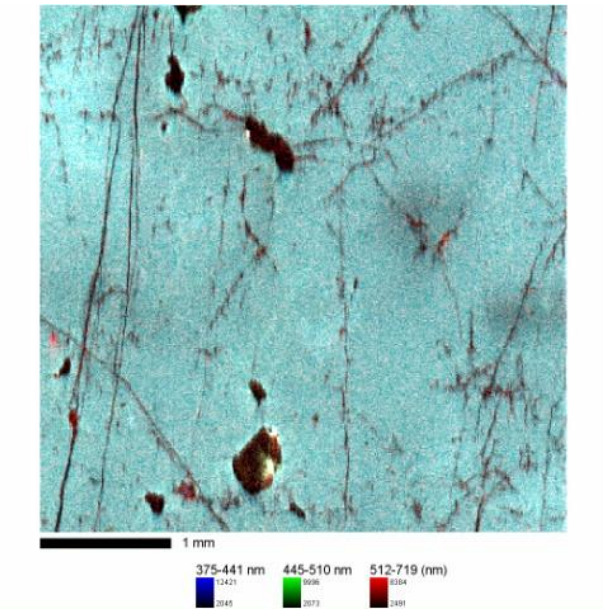


**Figure 18: SEM-CL image of thin section 016 (M. Raanes, S. Hagen 2011)**

#### 5.3.2.3 024

PTS 024 has a very light feldspar, which causes the image to be rendered too darkly, and the quartz to become very gray. This figure , Figure 19, does show that the quartz may be darker along the grain boundaries, which indicates a low temperature, slowly crystallizing event. Still, all of the quartz grains are of the same color, indicating one single crystallization.

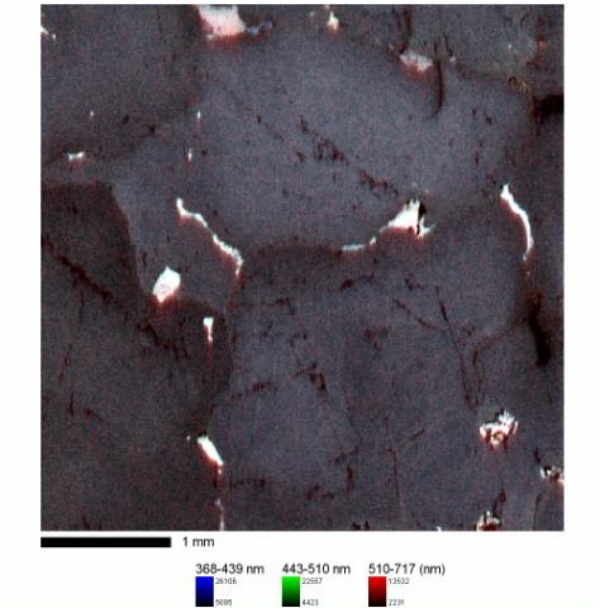


**Figure 19: SEM-CL image of thin section 024 (M. Raanes, S.Hagen, 2011)**

#### 5.3.2.4 Apl-1B

PTS Apl-1B has such a luminescent feldspar that the entire Figure 20 is disturbed. This sample is, unlike the former three, collected by Jacamon (2006), and is sampled from the aplite in which the quartz vein samples lie. By this image alone it is not possible to determine whether the quartz in the aplite and the quartz in the veins are crystallized simultaneously.

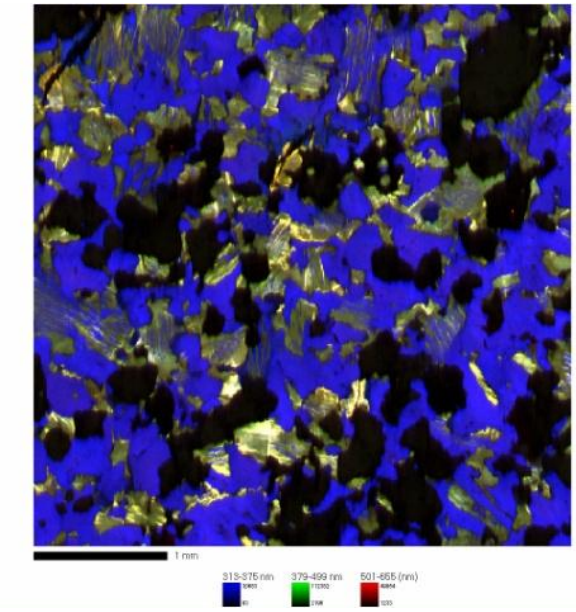

**Figure 20: SEM-CL image of thin section Apl-1B (M. Raanes, S. Hagen, 2011)**

#### 5.3.3.1 SEM-CL of FS

The following samples that are all made into and analyzed on polished thick sections have the same thresholds (+- 6), with the blue color representing the spectra of 174 to 420 nm, green representing the spectra of 420 – 500 nm and the red representing the spectra of 500 – 882 nm. The threshold values are chosen based on experimentation to get the most easily readable images.

#### 5.3.3.2 012

Figure 21 shows the imaging of a first generation impression of quartz with hints of zonation towards the edges, and feldspars with very strong CL-interference. The dark, tiny spots and lines throughout the quartz are primary and secondary fluid inclusions.

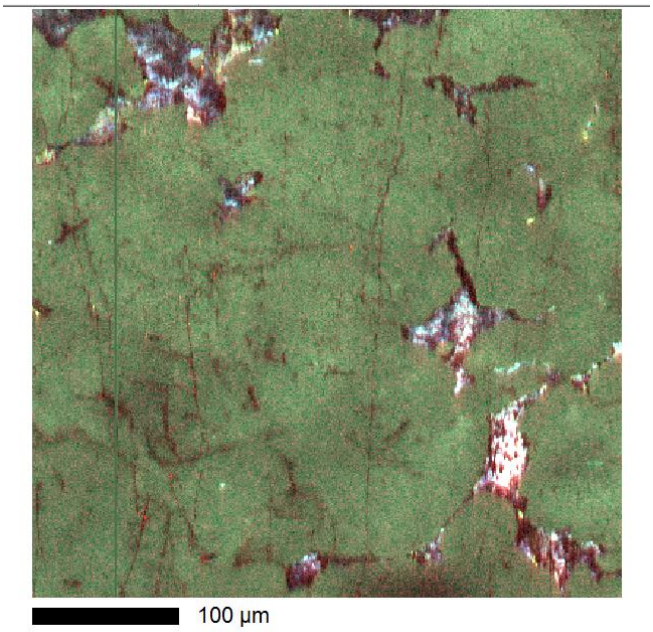


**Figure 21: SEM-CL image of thick section 012 (M. Raanes, S. Hagen, 2011)**

#### 5.3.3.3 016

Figure 22 shows a thick section from sample 016. The quartz looks homogenous and of a first generation origin, and the lighter zones are probably due to there not being very many fluid inclusions in the areas. The smaller dark spots and lines are again fluid inclusions. The larger dark and red spots are feldspar grains.

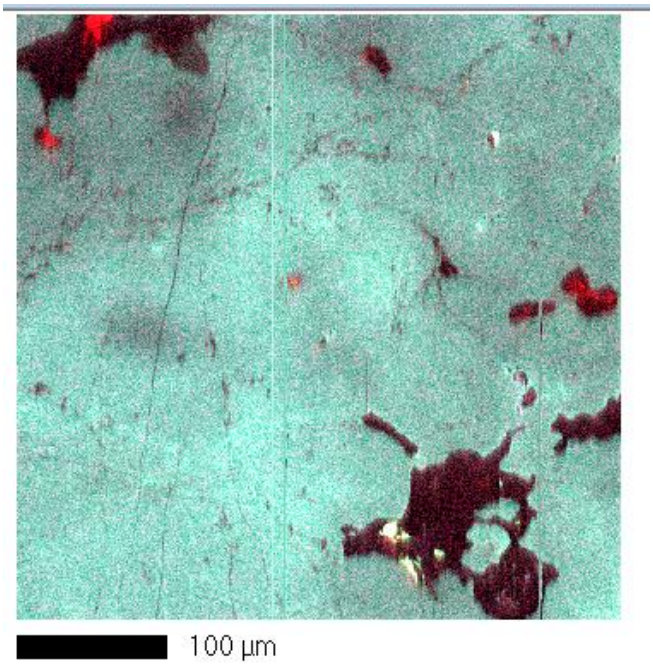


**Figure 22: SEM-CL of thick section 016 (M. Raanes, S. Hagen, 2011)**

#### 5.3.3.4 024

A SEM-CL of a thick section from sample 024 is shown in Figure 23. This is, like the former ones, a fairly homogenous quartz with some zonation along the edges. The straight, white vertical line is due to a software error. The primary fluid inclusions are not very dominating here compared to the other images, and the secondary inclusions.

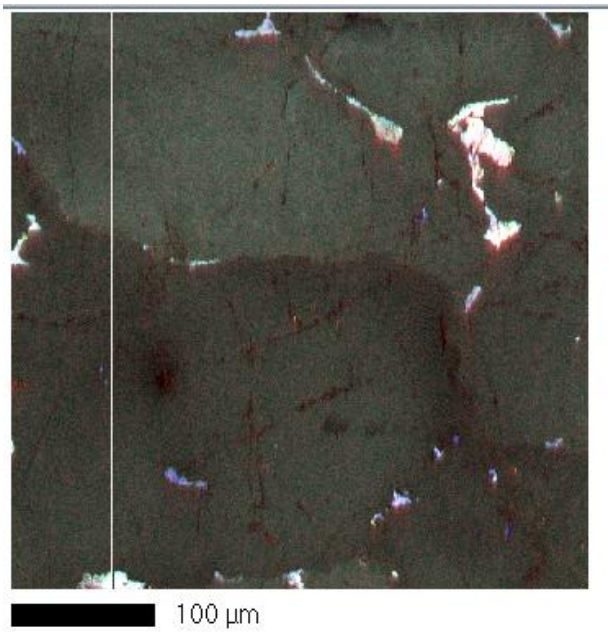


**Figure 23: SEM-CL image of thick section 024 (M. Raanes, S. Hagen, 2011)**

## 5.4 Microthermometry

### 5.4.1 Introduction

The microthermometry experiments were performed over a course of two months. Five thick sections were initially chosen for the experiments, with one of them being a thick section collected by F. Jacamon. The areas chosen within the thick sections are intended to be restricted to the areas imaged in the figures under Chapter 5.3, but due to a lack of large enough inclusions in some of the areas, these are excluded from the study. As the purpose of the SEM-CL in large was to determine the number of quartz generations, and they seem to be all from one (primary) generation, the areas chosen for the microthermometry are not very important. What might be more important is the difference between the primary and secondary inclusions, and also the differences between the types of fluid inclusions, and the similarities within these groups.

The fluid inclusions found in the quartz veins can be divided into four types by visual inspection at room temperature, and these have their own set of range temperatures for the different fluid inclusion parameters. For a full list over fluid inclusions, types and temperatures, please refer to the Appendix.

### 5.4.2 $H_2O$-rich fluid inclusions

Table 5 shows the parameters and statistics for the two-phase $H_2O$ inclusions.

| Two-phase H2O | Min. value | Max. Value | Average | Mean | Comment |
|---|---|---|---|---|---|
| *T* (freeze) | -39 | -39 | -39.0 | -39 | 4 records |
| *T*m ini | -30 | -10.7 | -19.7 | -19.15 | 4 records |
| *T*m CO2 | -42 | -13 | -22.3 | -20.4 | |
| *T*m H2O | -18.5 | 6.8 | -5.8 | -5.4 | |
| *T*h H2O | 154.3 | 247.5 | 187.4 | 184.3 | |
| % vapor of inclusion | 9.7 | 20 | 13.9 | 13.2 | |
| Area of inclusion | 17.5 | 212.8 | 72.1 | 47.1 | |

These fluid inclusions are generally the largest of the inclusion found in the thin sections, ranging from 17.5 to 212.8 $\mu m^2$, and having an average area of 72 $\mu m^2$. These inclusions were also by far the most common, and easier than the other kinds to classify due to their relatively large size and only two phases. An example of $H_2O$-rich fluid inclusions can be found in Figure 24.

The *T* (freeze) is the temperature in degrees Celsius where the entire inclusion is frozen over, which will happen quite abruptly. All of the inclusions that were measured showed a freezing temperature of -39 degrees, making all of the values in Table 5 equal. Realistically all inclusions of approximately the same size coming from the same phase cooled with the same procedure should freeze almost at the same time. Seeing as the inclusions are not all of the same size and that there might have been variations in the cooling processes due to malfunctioning equipment, the given result is to be administered with a pinch of salt.

**Figure 24: The largest of the two-phase H2O-rich FI, appx. 15µm along the longest axis. Also showing are some smaller CO2-rich FI. (S. Hagen, 2011)**

$T_m$ ini denotes the point of initial melting of the fluid inclusion. This is a property that was found to be extremely difficult to pinpoint, and it cannot be ruled out that the initial melting might have a margin of error of at least one degree. This is due to the initial melting probably occurring along the margins of the fluid inclusions first, making a tiny rim which might be very hard to see before more of the inclusion has melted.

$T_m$ $CO_2$ occurs when all of the $CO_2$ in the inclusion appears to be melted.

$T_m$ $H_2O$ occurs when all of the $H_2O$ in the inclusion appears to be melted. As the results here have an average melting temperature of less than 0°C, it indicates that the $H_2O$ is enriched in salts.

The homogenization temperature of $H_2O$ is measured in between 154 and 247°C, which is a quite large span.

Processing the data through the programs BULK and ISOC (Bakker, 2011), the volume fractions and densities of the fluid inclusions are taken into account. This provides an isochore as shown in Figure 25.

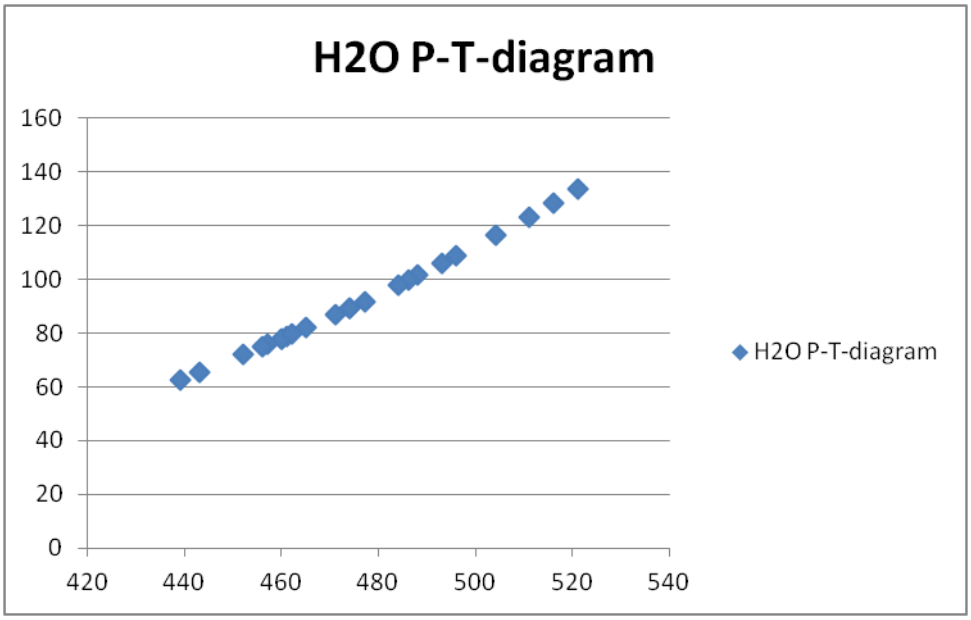


**Figure 25: Isochore based on BULK and ISOC calculations from the H2O fluid inclusions data. The label of the x-axis is Temperature in K, the label of the y-axis is Pressure in MPa.**

The figure shows a clear linear correlation between the temperature and pressure data of the inclusion.

### 5.4.3 $CO_2$-rich, two-phase fluid inclusions

Table 6 shows the parameters and statistics for the two-phase $CO_2$ inclusions.

| Two-phase CO2 | Min. value | Max. Value | Average | Mean | Comment |
|---|---|---|---|---|---|
| *T* (freeze) | -100 | -92 | -95.7 | -95 | |
| *T*m CO2 | -59 | -57 | -58.4 | -58.7 | |
| *T*h CO2 | -0.2 | 25.5 | 15.9 | 17.7 | |
| % vapor of inclusion | 58.5 | 59.1 | 58.8 | 58.8 | 2 records |

The freezing temperature found in Table 6 is quite a bit lower than for the $H_2O$-rich fluid inclusions, which should be expected. The melting and homogenization temperature is also lower, and the vapor to liquid-ratio is higher based on areas of the vapor bubble and the inclusion itself at room temperature. Due to all of this, the temperature and pressure diagrams, along with the estimated density by the BULK programme, gives a quite different, but still linear isochore, shown in Figure 26.

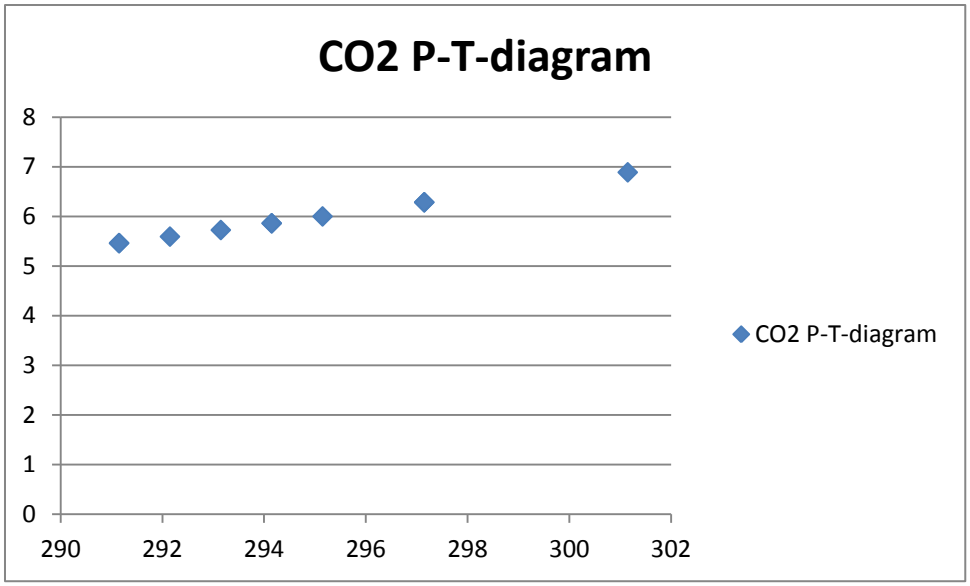


**Figure 26: Isochore made from fluid inclusion data from the CO2-rich fluid inclusions. The x-axis denotes Temperature in K, and the y-axis denotes Pressure in MPa.**

### 5.4.4 $CO_2$-rich, three-phase fluid inclusions

Table 7 shows the parameters and statistics for the three-phase $CO_2$ inclusions.

| Three-phase CO2 | Min. value | Max. Value | Average | Mean | Comment |
|---|---|---|---|---|---|
| *T* (freeze) | -98 | -95 | -96.7 | -97 | |
| *T*m CO2 | -58.7 | -56.7 | -57.3 | -57.2 | |
| *T*m clath | 1.8 | 9.5 | 6.8 | 7.6 | |
| *T*h CO2 | 17.9 | 27.8 | 21.9 | 21.7 | |
| *T*h H2O | 242.8 | 242.8 | 242.8 | 242.8 | 1 record |
| % vapor of inclusion | 20.8 | 86.6 | 54.8 | 62.7 | |

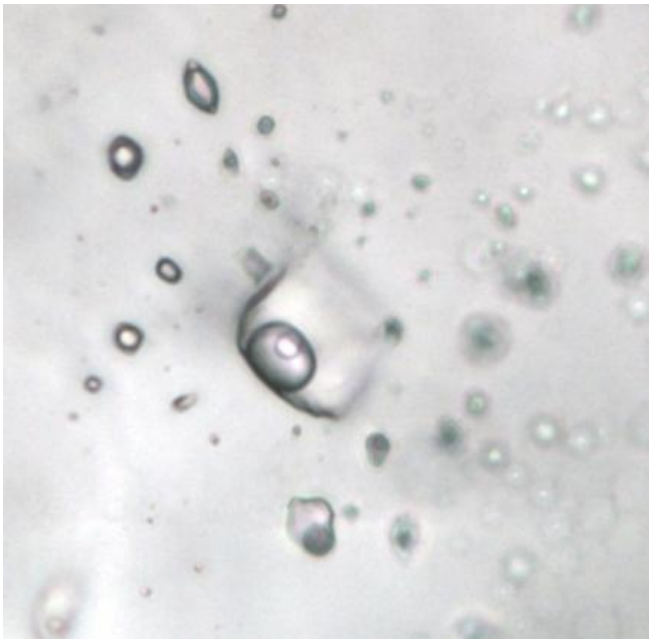

**Figure 27: Three-phase CO2-rich fluid inclusion. Smaller, two-phase CO2-rich inclusions in top left corner. (S.Hagen, 2011)**

### 5.4.5 NaCl-rich fluid inclusions

Table 8 shows the parameters and statistics for the three-phase $H_2O$ inclusions.

| Three-phase H2O-rich | Min. value | Max. Value | Average | Mean | Comment |
|---|---|---|---|---|---|
| *T*m ini | -65.2 | -27 | -46.1 | -46.1 | 2 records |
| *T*m clath | -53.4 | -28.9 | -41.8 | -41.3 | |
| *T*h CO2 | 147.3 | 185.5 | 167.9 | 166.6 | |
| *T*h salt | 145 | 229.1 | 203.1 | 217.2 | 5 records |

The three-phase fluid inclusions were seldomly found, but when found appeared in great extent. Figure 28 shows at least 10 easily recognizable cubic, colorless halite crystals. They appeared smaller than the regular two-phased $H_2O$-inclusions and were therefore harder to measure. Measuring difficulties are the cause of the few records found in Table 8, but the ones obtained showed interesting results with very differing homogenizing temperatures. Comparing with Table 3, it is apparent that the large difference in homogenization temperature only gives a very small difference in salinity.

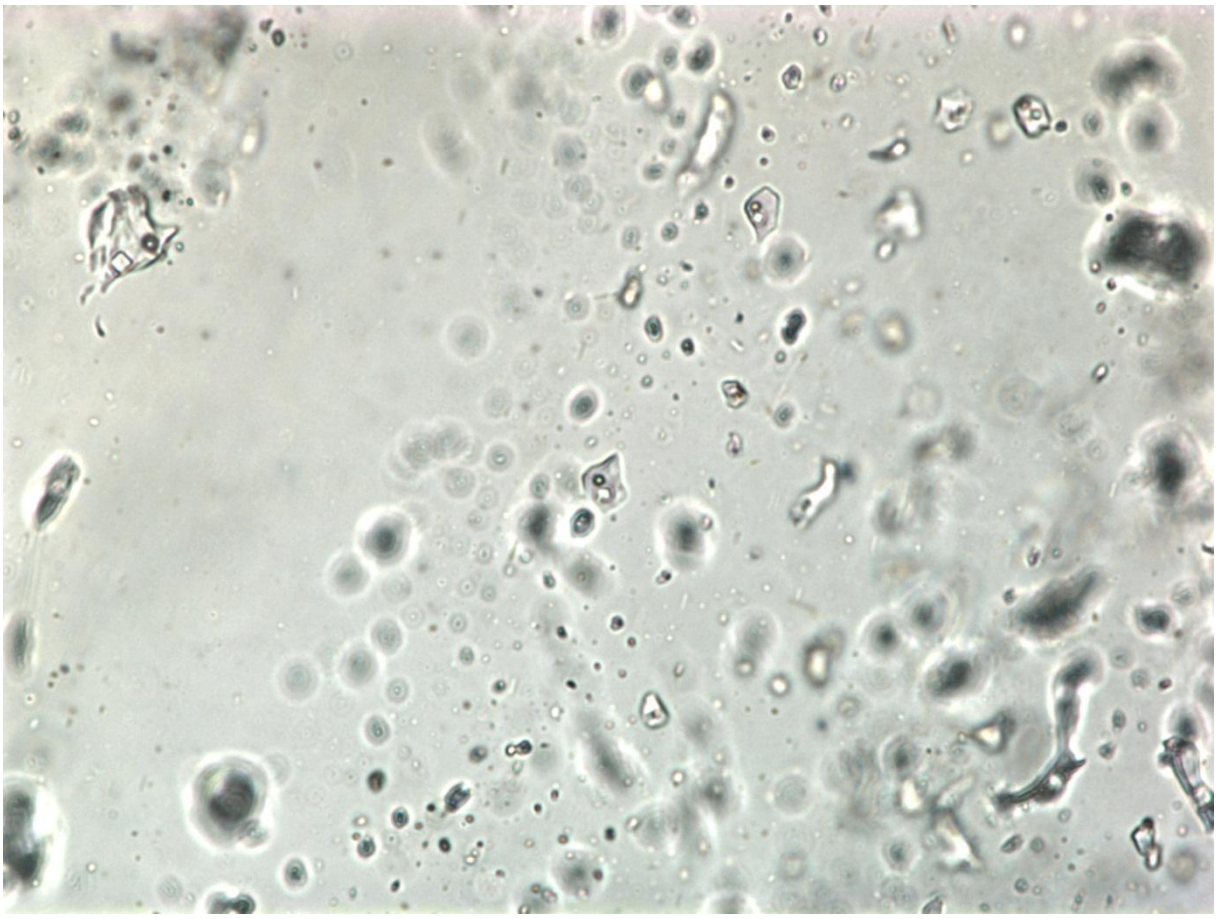

**Figure 28: Salt-rich (three phase) H2O-rich fluid inclusions (S. Hagen, 2011)**

# Discussion

## 6.1 The possibility of a Mo-enriched fluid phase in the Kleivan Granite

Earlier work by Barstad (2011) indicates that if there is any Mo in the Kleivan granite, it is either in the quartz veins in the aplitic roof zone, or it has escaped into the surrounding rocks. It is suspected that the mineralization therefore is closely related to fluid inclusions as no Mo is to be found in the veins themselves. Madsen found salt-rich fluid inclusions in his samples in 1977, but mainly in the northern and the central zones.

## 3.10 Salinities in the Kleivan quartz veins

As shown in the results in Chapter 5, four types of inclusions have been found, with different characteristics. It is felt that the main focus should be on the $H_2O$-rich two-phased inclusions and also the three-phased $H_2O$-rich inclusions containing salt crystals. Based on the data found in Tables 2 and 3 in Chapter 4 Theory, and Tables 5 and 8 in Chapter 5 Results, the following salinities have been obtained:

The melting temperature of $H_2O$ in the two-phased inclusions varies from -18.5 °C all the way up to 6,8°C. The positive melting temperature can not readily be explained without further research, but it is without question a valid result as it has happened several times in different sections. The average melting temperature, however, is -5.8°C and the mean -5.4°C, giving us a maximum salinity for the inclusions at up to 21.3 wt% NaCl, with an average around 8.5 wt%.

The melting temperature of the salt crystals have been obtained where possible, and in 5 instances, it was. The melting temperature varies from 145°C up to 229.1°C, with an average at 203.1°C and a mean temperature of 217.2°C. This gives, according to Table 3, salinities from 28.5 up to 32.2 mass% NaCl-equivalents.

## 3.11 Comparison to the salinities from the Madsen study

Madsen (1977) divides the inclusions found in the entire granite into three types, which are the same that are found here, but in this study the NaCl-rich inclusions are separated as a distinct type, instead of being a subgroup of the $H_2O$-rich two-phased inclusions.

The inclusions are not directly comparable as the focus of this study has been the quartz veins only while Madsen sampled the entire chamber. The salinities are very similar, though, and with Madsen suspecting a secondary origin for all of his inclusions, the inclusions of this

study has been primary. This could either mean that there were two pulses of very similar salinities, going once through the entire granite and once forming as the quartz veins in the top of the chamber in the very south. The quartz veins in the top of the chamber are assumed to be contemporaneous of the rest of the chamber, but this may be wrong. In that case, it would not be entirely unlikely that a hydrothermal fluid-pulse went through the chamber after it was fully or nearly fully formed in the lower parts, and collecting in the half-consolidated top part of the chamber.

If the quartz veins are contemporaneous, a second hydrothermal pulse may have come, of unclear origin, and lead to the formation of the fluid inclusions in the rest of the chamber. Or it might have been the same fluids all along, but that would go against Barstads (2011) hypothesis of the formation of a hydrothermal fluid phase because the saline fluids should have been enriched in the end instead of being compatible in the melt at the time of formation. A more thorough comparison of quartz generations may give an answer to this question.

## 3.12 Comparison to the Questa Porphyry Mo deposit

The Questa deposit is a lot younger than the Kleivan granite, giving less time to "wash out" any mineralization. The Questa shows molybdenite at a microscopic level, and despite having some rather large and saline brine inclusions (Klemm, Pettke, & Heinrich, 2008), the salinities of the hydrothermal part of the MHBX matrix are between 3 and 8.5 wt%, so quite smaller than the salinities found both in the Kleivan granite itself and its stockwork veins. The Questa has several generations of quartz formation, with the Kleivan apparently only having one.

## 6.5 Suggested additional work

As usual, the limiting factors for this project have been time and resources, so for further work it is suggested to get a better overview of the salt-rich fluid inclusions of the Kleivan granite, and especially measure them. A lot of data has been rendered un-usable due to misunderstandings about the importance of liquid/vapor ratio.

A comparison between the fluid inclusions of the quartz veins and the aplite granite was abandoned due to time limitations, but it could have been interesting to investigate whether the fluid inclusions and the quartz formation in the two are contemporaneous.

It would also be interesting to figure out why the $H_2O$ fluid inclusions show such a high pressure compared to the relatively normal pressure levels of the $CO_2$, and almost certainly there is value in learning to know the programs from Bakker better.

A very possible and useful tool to use in further investigations of the Kleivan granite and fluid inclusions in general is LA-ICP-MS, which is a commonly used method in all papers published in the last years. It would be able to detect trace elements, one of them being Mo, and could very possibly give the (possibly very much more expensive) desired results.

# 7 Conclusion

The macroscopic analyses did not indicate any other minerals of significance other than the described quartz, altered feldspar and biotite. This suggests that there are no Molybdenum mineralizations of any significance in the quartz veins in the top of the Kleivan aplite granite.

The intended purpose of the SEM-CL-analysis was to investigate whether the quartz in the veins were formed in several outbursts, heavily recrystallized within the vein or just formed by one single crystallization process. For the eight samples processed, the results indicate that there were only one crystallization, and only slight zonation in some grains. This indicates that of the samples processed, all of them came from the same crystallization process, and by explanation of the Burnham model in Chapter 4, this should have happened at the end of the crystallization of the chamber.

The microthermometry showed mostly consistent results with salinities comparable to the ones obtained by Madsen. The Kleivan granite shows many dissimilarities to the Questa porphyry, but the possibility of finding more similarities between the two cannot be excluded.

The salt-rich fluid inclusions gives a further impression of a primary set of fluid inclusions contained within the quartz crystallizing at the final stage of the cooling and fractioned crystallization of the Kleivan granite, and with salinities from roughly 8 - 32wt% it is possible that some interesting elements may be a part of these.

At this point it is not possible to determine whether the Kleivan granite is a possible future source for molybdenum, but with further examinations, maybe with the help of LA-ICP-MS, it seems very likely that very trustworthy results can be obtained.

# References


Audétat, A., Dolejš, D., & Lowenstern, J. B. (2011, March 31). Molybdenite Saturation in Silicic Magmas: Occurrence and Petrological Implications. *Journal of Petrology Advance Access* , ss. 1-14.

Bakker, R. J. (2011). *Fluid inclusions; Critical review, applications, computer modeling. Short course.* Leoben: University of Leoben, Austria.

Barstad, Å. E. (2011). *Molybdenittmineraliseringer i Kleivangranitten, Lyngdal (MSc-thesis).* Trondheim: NTNU.

Geological Survey of India. (u.d.). *Standard operating procedure - Fluid inclusion studies.* Hentet September 15, 2012 fra http://www.portal.gsi.gov.in/gsiDoc/pub/final_sop_fluid_inclusion_lab.pdf

Jacamon, F., & Larsen, R. B. (2006a, August). Trace element evolution in quart during fractional crystallization of the high T and P charnockittic Kleivan granite, south-western Norway. *The significance of textures and trace element chemistry of quartz with regard to the petrogenesis of granitic rocks, Ph.D-thesis* , ss. 1-38.

Klemm, L., Pettke, T., & Heinrich, C. (2008). Fluid and source magma evolution of the Questa porphyry Mo deposit, New Mexico, USA. *Miner Deposita 43* , ss. 533-552.

Knaben.no. (u.d.). *knaben.no*. Hentet 05 15, 2012 fra http://www.knaben.no

Ludington, S., & Plumlee, G. (2009, 12 15). Climax-type Porphyry Molybdenum Deposits. *Open-File Report, United States Geological Survey* , ss. 1-13.

Madsen, J. (1977, June). Composition and microthermometry of fluid inclusions in the Kleivan granite, South Norway. *American Journal of Science* , ss. 673-696.

NTNU. (2008, March 5). *JEOL JXA-8500F Electron Probe Micro analyzer (EPMA).* Hentet September 29, 2012 fra http://www.material.ntnu.no/lab/material/equipment/ProdInfoEPMA.pdf

Petersen, J. S. (1980). The zoned Kleivan granite - an end member of the anorthosite suite in southwest Norway. *Lithos 13* , ss. 79-95.

Raanes, M. P. (2012, May). Personal message.

Ramberg, I. B., Bryhni, I., & Nøttvedt, A. (2007). *Landet blir til (The Making of a Land).* Trondheim: Norsk Geologisk Forening.

Robb, L. (2005). *Introduction to ore-forming processes.* Blackwell Publishing.

Roedder, E., & Bodnar, R. (1980). Geologic pressure determinations from fluid inclusion studies. *Ann. Rev. Earth Planet Science 8th issue* , ss. 263-301.

trainor.no. (2011). *HMS in the laboratory*.

University of Wisconsin. (2004). *Volcanic Violence*. Retrieved September 29, 2012, from Whyfiles.org, website for the University of Wisconsin: http://whyfiles.org/031volcano/2.html

Vander Auwera, J., Bolle, O., Bingen, B., Liégeois, J.-P., Bogaerts, M., Duchesne, J., et al. (2011, April 15). Sveconorwegian massif-type anorthosites and related granitoids result from post-collisional melting of a continental arc root. *Earth-Science Reviews 107* , ss. 375-397.

# Appendix:

# Full list of microthermometry results

| Inclusion | # of phases | Type | T (freeze) | Tm CO2 | Tm H2O | Tm LG- L | Th CO2 | Td | T min |
|---|---|---|---|---|---|---|---|---|---|
| D03 | 2 | H2O | | -15 | 6.8 | 214.7 | | | -190 |
| D04 | 2 | H2O | | -15 | 5.9 | 223.4 | | | -190 |
| D05 | 2 | H2O | | | -5.4 | 187.7 | | | -115 |
| D06 | 2 | H2O | | | -5.4 | 187.3 | | | -115 |
| D07 | 2 | H2O | | | -5 | 179 | | | -119 |
| D08 | 2 | H2O | | -15 | -5 | 187 | | | -190 |
| D09 | 2 | H2O | | | -6.1 | 201.4 | | | -117 |
| D10 | 2 | H2O | | | -4 | 184.3 | | | -117 |
| D11 | 2 | H2O | | | -4.9 | | | | -140 |
| D12 | 2 | H2O | | | -5.4 | 182.6 | | | -140 |
| D14 | 2 | H2O | | | -5.5 | 203.5 | | | -113 |
| D16 | 2 | H2O | | | -5.4 | 188.9 | | | -117 |
| D17 | 2 | H2O | | | -4.6 | 191.5 | | | -135 |
| D18 | 2 | H2O | | | -2.2 | 247.5 | | | -135 |
| D19 | 2 | H2O | | -16.2 | 4.4 | 200.7 | | | -130 |
| D21 | 2 | H2O | | | | 220.1 | | | -160 |
| D22 | 2 | H2O | | | | | | | -160 |
| D23 | 2 | H2O | | | 4.6 | 198 | | | -190 |
| D24 | 2 | H2O | | | 4.9 | 230.9 | | | -190 |
| D25 | 2 | H2O | | -13 | | | | | -130 |
| B01 | 2 | H2O-rich | -39 | | -5.4 | 212.7 | | | -180 |
| B02 | 2 | H2O-rich | -39 | | -5.4 | 211 | | >250 | -180 |
| B03 | 2 | H2O-rich | -39 | | -5.4 | 238.5 | | | -180 |
| B04 | 2 | H2O-rich | -39 | | -5.4 | | | >250 | -180 |
| B08 | 2 | H2O-rich | | | -4.4 | 170 | | | -190 |
| B09 | 2 | H2O-rich | | | -3.9 | 166.4 | | | -190 |
| B17 | 2 | H2O-rich | | -26.4 | -18 | | | | -150 |
| B18 | 2 | H2O-rich | | | -17.3 | | | | -150 |
| B19 | 2 | H2O-rich | | | | | | | -125 |
| B20 | 2 | H2O-rich | | | -9.6 | | | | -125 |
| B24 | 2 | H2O-rich | | | -5.3 | 212.6 | | | -160 |
| B30 | 2 | H2O-rich | | | -8 | | | | -150 |

| | | | | | | | | | |
|---|---|---|---|---|---|---|---|---|---|
| B32 | 2 | H2O-rich | | | | 164.7 | | | |
| B33 | 2 | H2O-rich | | | | 176 | | | |
| B34 | 2 | H2O-rich | | | | 176 | | | |
| B35 | 2 | H2O-rich | | -24.7 | -15.7 | | | | -120 |
| B36 | 2 | H2O-rich | | -26.4 | -15.7 | | | | -120 |
| B37 | 2 | H2O-rich | | -42 | -16.1 | | | | |
| C32 | 2 | H2O-rich | | | -5.2 | | 161.5 | | |
| C33 | 2 | H2O-rich | | | -5.2 | | 160.5 | | -185 |
| C34 | 2 | H2O-rich | | | -6.3 | | 158.9 | | -185 |
| C36 | 2 | H2O-rich | | | -5.6 | | 162.4 | | -185 |
| C37 | 2 | H2O-rich | | | -5.6 | | 160 | | -185 |
| C45 | 2 | H2O-rich | | | -5.5 | | 159.8 | | -178 |
| C46 | 2 | H2O-rich | | | -5.5 | | 161.9 | | -178 |
| C47 | 2 | H2O-rich | | | -5.8 | | 154.3 | | -178 |
| C48 | 2 | H2O-rich | | | -5.8 | | 169.3 | | -178 |
| C49 | 2 | H2O-rich | | | -17.5 | | 164.4 | | -178 |
| C50 | 2 | H2O-rich | | | -18.5 | | 159.6 | | -178 |
| B21 | | | | -29.8 | -16.3 | | | | -140 |
| B22 | | | | | | | | | |
| D38 | | | | | -1.3 | 184 | | | -145 |
| D40 | | | | | 3.2 | 197.7 | | | -145 |
| D44 | | | | | -1.2 | 180.9 | | | -145 |
| D45 | | | | | -3.3 | 191.9 | | | -145 |

| Inclusion | # of phases | Type | T (freeze) | Tm (ini) | Tm H2O | Tm clath | Tm LG- L | Th CO2 | Td | T min |
|---|---|---|---|---|---|---|---|---|---|---|
| B31 | 3 | H2O-rich + smth | | -27 | -7.7 | | | | | -150 |
| C35 | 3 | NaCl-rich | | | | -41.3 | 145 | 147.3 | | -185 |
| C38 | 3 | NaCl-rich | | | | -51.9 | >280 | 168.2 | | -190 |
| C39 | 3 | NaCl-rich | | | | -53.4 | 219.4 | 166.6 | | -190 |
| C40 | 3 | NaCl-rich | | | | -53.2 | 204.7 | 165.5 | | -190 |
| C41 | 3 | NaCl-rich | | | | -28.9 | | | | -185 |
| C42 | 3 | NaCl-rich | | | | -34.1 | | 172.6 | | -185 |
| C43 | 3 | NaCl-rich | | | | -29.4 | | 178.9 | | -190 |
| C44 | 3 | NaCl-rich | | | | -30.7 | | 162.9 | | -190 |
| C51 | 3 | NaCl-rich | | | | | 229.1 | 185.5 | | -190 |
| C52 | 3 | NaCl-rich | | -65.2 | | -53.3 | 217.2 | 163.6 | | -190 |
| | | | | | | | | | | |
| | | | | | | | | | | |
| B11 | 3 | H2O-rich | | -25 | -10.2 | | | | >250 | -195 |
| B23 | 3 | H2O-rich | -45 | | -5.3 | | | | >250 | -160 |

| Inclusion | # of phases | Type | T (freeze) | Tm CO2 | Tm clath | Th CO2 | T min |
|---|---|---|---|---|---|---|---|
| D02 | 2 | CO2 | -97 | -59 | 7.1 | 21.4 | -150 |
| D13 | 2 | CO2 | | -58.8 | | 19.9 | -140 |
| D39 | 2 | CO2-rich | | -58.3 | | 7.8 | -145 |
| B27 | 1 | CO2 | -92 | -57 | | 2 | -145 |
| B28 | 1 | CO2 | -92 | -57 | | 3.5 | -145 |
| B29 | 1 | CO2 | -92 | -57 | | -0.2 | -145 |
| D26 | 1 | CO2 | -95 | -58.7 | | 22.9 | -155 |
| D27 | 1 | CO2 | -95 | -58.7 | | 17 | -155 |
| D28 | 1 | CO2 | -95 | -58.7 | | 17.7 | -155 |
| D29 | 1 | CO2 | -95 | -58.7 | | 17.3 | -155 |
| D30 | 1 | CO2 | -95 | -58.7 | | 25.5 | -155 |
| D31 | 1 | CO2 | -95 | -58.7 | | 17.3 | -155 |
| D32 | 1 | CO2 | -95 | -58.7 | | 20.3 | -155 |
| D33 | 1 | CO2 | -100 | -58.7 | | 22.2 | -190 |
| D34 | 1 | CO2 | -95 | -58.7 | | 22.8 | -155 |
| D35 | 1 | CO2 | -95 | -58.7 | | 21.8 | -155 |
| D36 | 1 | CO2 | -98 | -58.1 | | 17.8 | -190 |
| D37 | 1 | CO2 | -98 | -58.1 | | 9.4 | -190 |
| D41 | 1 | CO2 | -98 | -58.7 | | 21.4 | -155 |
| D42 | 1 | CO2 | -98 | -58.7 | | 21 | -155 |
| D43 | 1 | CO2 | -98 | -58.1 | | 23 | -190 |
| D46 | 1 | CO2-rich | | -57.9 | | 15.8 | -145 |
| D47 | 1 | CO2-rich | | -58.3 | | 6.4 | -145 |
| D48 | 1 | CO2-rich | | | | | -120 |
| D49 | 1 | CO2-rich | | -58.1 | | 10.8 | -120 |
| D50 | 1 | CO2-rich | | -58.8 | | 13.4 | -120 |
| | | | | | | | |
| | | | | | | | |
| D20 | 3 | CO2 | | -58.7 | 1.9 | 23 | -190 |
| | | | | | | | |
| B05 | 3 | CO2-rich | -98 | -57.7 | 6.9 | | -190 |
| B06 | 3 | CO2-rich | -95 | -57.7 | | | -190 |
| B07 | 3 | CO2-rich | -95 | -57.7 | 6.1 | | -190 |
| B10 | 3 | CO2- | | -57.4 | 1.8 | 27.8 | -140 |

| | | | | | | | |
|---|---|---|---|---|---|---|---|
| | | rich | | | | | |
| B12 | 3 | CO2-rich | -97 | -57.1 | 9 | 18.1 | -175 |
| B13 | 3 | CO2-rich | -97 | -56.7 | 8.9 | 17.9 | -130 |
| B14 | 3 | CO2-rich | -97 | -56.7 | 8.9 | 19.2 | -130 |
| B15 | 3 | CO2-rich | -97 | -57 | 9.2 | 23.5 | -175 |
| B16 | 3 | CO2-rich | | -57.1 | 4.1 | 23.6 | -130 |
| B25 | 3 | CO2-rich | -97.5 | -57.2 | 8.3 | 24 | -195 |
| B26 | 3 | CO2-rich | -97.5 | -57.2 | 9.5 | 21.4 | -195 |